Variational Anonymous Quantum Sensing

Muhammad Shohibul Ulum, Uman Khalid, Jason William Setiawan, Trung Q. Duong, *Fellow, IEEE*, Moe Z. Win, *Fellow, IEEE*, and Hyundong Shin, *Fellow, IEEE*

***Abstract*—Sensing networks play an important role in delivering high-quality services for emerging applications in wireless networks, such as seamless immersive experiences and real-time surveillance. Notably, sensing networks feature the sharing of sensing information among the network parties, which renders the importance of ensuring the security and privacy of sensing data, especially in applications involving the exchange of privacy-sensitive data. These applications demand ultra-reliable, ultra-secure, ultra-precise sensing and hyper-accurate measurements. However, classical sensing networks are limited in their precision, security, and privacy. Quantum sensing networks (QSNs) incorporate quantum sensing and quantum communication to achieve Heisenberg precision and unconditional security by leveraging quantum properties such as superposition and entanglement. The QSN deployment of noisy intermediate-scale quantum (NISQ) devices faces the near-term practical challenges. In this paper, we employ variational quantum sensing (VQS) to optimize sensing configurations in noisy environments for the physical quantity of interest, e.g., magnetic-field sensing for navigation, localization, or detection. The VQS algorithm is variationally and evolutionarily optimized using a genetic algorithm to tailor a variational or parameterized quantum circuit (PQC) structure that effectively mitigates quantum noise effects. This *genetic* VQS algorithm designs the PQC structure to create a variational probe state that outperforms the maximally entangled or product quantum state under bit-flip, dephasing, and amplitude-damping quantum noise for both single-parameter and multiparameter NISQ sensing, specifically as quantified by the quantum Cramér–Rao bound. Furthermore, we incorporate the quantum anonymous broadcast (QAB) to anonymously share the sensing information in the VQS network, ensuring anonymity and untraceability of sensing data. We further analyze the broadcast bit error probability (BEP) for the QAB protocol under quantum noise, showing its robustness—i.e., *error-free* resilience—against bit-flip noise as well as the *low-noise* BEP behavior. This work provides a scalable framework for integrated quantum anonymous sensing and communication, particularly in a *variational* and *untraceable* manner.**

***Index Terms*—Integrated sensing and communication, quantum anonymous communication, quantum Cramér–Rao bound, variational quantum sensing.**

ACRONYMS

BEP	Bit error probability
CNOT	Controlled-NOT
CPTP	Completely positive trace-preserving
GA	Genetic algorithm
GHZ	Greenberger–Horne–Zeilinger
IoT	Internet of Things
ISAC	Integrated sensing and communication
NISQ	Noisy intermediate-scale quantum
PQC	Parameterized quantum circuit
QAB	Quantum anonymous broadcast
QAC	Quantum anonymous communication
QAS	Quantum anonymous sensing
QCRB	Quantum Cramér–Rao bound
QFI	Quantum Fisher information
QFIM	Quantum Fisher information matrix
QSN	Quantum sensing network
SQL	Standard quantum limit
VQA	Variational quantum algorithm
VQS	Variational quantum sensing

M. S. Ulum, U. Khalid, J. W. Setiawan, and H. Shin are with the Department of Electronics and Information Convergence Engineering, Kyung Hee University, 1732 Deogyeong-daero, Giheung-gu, Yongin-si, Gyeonggi-do 17104 Korea (e-mail: hshin@khu.ac.kr).

T. Q. Duong is with the Faculty of Engineering and Applied Science, Memorial University of Newfoundland, Canada, and also with the School of Electronics, Electrical Engineering and Computer Science, Queen's University Belfast, Belfast BT7 1NN, UK (e-mail: trung.q.duong@qub.ac.uk).

M. Z. Win is with the Laboratory for Information and Decision Systems (LIDS), Massachusetts Institute of Technology, 77 Massachusetts Avenue, Cambridge, MA 02139 USA (e-mail: moewin@mit.edu).

I. INTRODUCTION

WIRELESS positioning and sensing is pivotal for the deployment of next-generation integrated sensing and communication (ISAC) technologies for augmented localization services, environmental monitoring, secure positioning, vehicular safety, real-time precise surveillance, and seamless immersive experiences [1]–[16]. These services require ultra-reliable, ultra-secure, and low-latency communications as well as ultra-precise sensing and hyper-accurate measurements. However, classical networks face fundamental limitations in achieving advanced levels of precision and security. For instance, an intrinsic limitation is imposed by the standard quantum limit (SQL), which states that the variance of measurement precision scales as $1/N$ for a network of N sensors [17]. Although this degree of precision is sufficient for diverse real-world applications, emerging fields, such as healthcare networks, augmented reality, virtual reality, gravitational wave detection, and autonomous vehicular networks, require even more precision [18]–[20]. Moreover, classical noise sources such as shot noise, which commonly scales as $1/\sqrt{N}$, can further undermine classical sensing networks, thereby reducing their accuracy. In addition, sensing network security based on computational encryption methods is highly prone to quantum attacks owing to perpetual quantum computing capabilities.

Quantum Internet of Things (IoT) incorporates both quantum sensing and quantum communication to further augment sensing and communication capabilities of classical IoT [21], [22]. The emerging paradigm not only improves precision in measuring physical quantities such as electric and magnetic fields but also invokes unconditional communication security by harnessing quantum properties such as superposition and entanglement. Herein, the achievable precision of an entangled quantum sensing network (QSN) is fundamentally limited by the *Heisenberg* limit, exhibiting $1/N^2$ scaling in the measurement precision variance [17], [23]. Nonetheless, deployments

of QSNs face hurdles, particularly the detrimental noise effects on quantum-enhanced precision. Noise sources, e.g., thermal fluctuations and particle loss, can markedly degrade quantum states essential for achieving the Heisenberg-limit precision, necessitating intricate noise mitigation and error correction strategies [24], [25]. In terms of security, post-quantum secure protocols have been posited for QSNs, employing lattice-based cryptographic schemes resilient to quantum attacks [26]. Consequently, quantum IoT embodies a potent platform for high-precision measurements while ensuring robust communication security against quantum threats. However, the limitations of noisy intermediate-scale quantum (NISQ) devices, especially concerning privacy leakage and quantum noise, hinder fully realizing the potential benefits of integrating quantum sensing and communication [27]–[29].

Variational quantum sensing (VQS) fully leverages the near-term quantum advantages while addressing inherent quantum noise effects as well as quantum device imperfections [30]–[34]. VQS algorithms are resource-efficient, taking into account the qubit count, gate depth, and robustness against quantum noise [35]. The algorithms iteratively adjust sensing configurations to optimize quantum sensing probes to precisely estimate physical quantities, such as magnetic field, electric field, frequency, and temperature, under noisy environments [35]. Employing such an entangled QSN equipped with hybrid quantum-classical optimization exhibits quantum advantage in outperforming classical methods for dynamic sensing environments. In cryptographic metrology, the QSNs are designed for specific security-oriented sensing tasks related to secure surveillance, privacy-preserving asset tracking, unauthorized object detection, and anonymous navigation [36], [37]. Herein, the location of stationary sensing nodes and the identity of mobile sensing nodes are sometimes highly relevant in addition to the private data itself. Therefore, the sensing nodes are required to operate in an anonymous mode while sharing the sensing information or estimated parameters with other network participants. Quantum anonymous communication (QAC) becomes a primary candidate in such scenarios, which ensures the sensing anonymity, disapproves unauthorized node access, limits spoofing by blocking malicious nodes, and renders the sensing nodes as untraceable [38]–[41]. Therefore, such integrated quantum anonymous sensing (QAS) and communication networks can be deployed to deliver improved precision, enhanced sensitivity, and sensing privacy in parallel with classical counterparts.

Specifically, in this paper, we propose an integrated framework incorporating VQS with quantum anonymous broadcast (QAB) for variational QAS networks, as shown in Fig. 1. By harnessing the power of quantum algorithms, VQS optimizes NISQ sensors to mitigate quantum noise effects and enhance measurement precision. In parallel, QAB introduces a privacy layer to QSNs, preserving the anonymity of sensing data. This ISAC framework promises to achieve both quantum-empowered sensing precision and privacy, addressing critical classical constraints in ISAC—with applications of navigation, localization, imaging, and detection (radar), for example. Our main contributions are summarized as follows.

- We begin by fundamentally introducing quantum sensing protocols and variational quantum algorithms (VQAs) to formally define VQS protocols for single-parameter and multiparameter sensing tasks in noisy environments. Since the search space for optimization is vast and poorly defined, we develop *genetic* VQS detailing a genetic algorithm (GA) approach to *variationally* and *evolutionarily* optimize parameterized quantum circuits (PQCs) for VQS state preparation in NISQ sensing, e.g., scalar and vector magnetic-field sensing.
- We provide metrologically resourceful ansatzes designed to create genetic VQS probe states that maximize measurement precision in terms of the quantum Fisher information (QFI) under anisotropic quantum noise such as the bit-flip, dephasing (or phase-flip), and amplitude-damping (or energy-relaxation) noise. These tailored VQS probe states exhibit high-sensitivity estimation capacity as quantified by the quantum Cramér–Rao bound (QCRB) under all inherent quantum noise, compared with maximally entangled Greenberger–Horne–Zeilinger (GHZ) or product

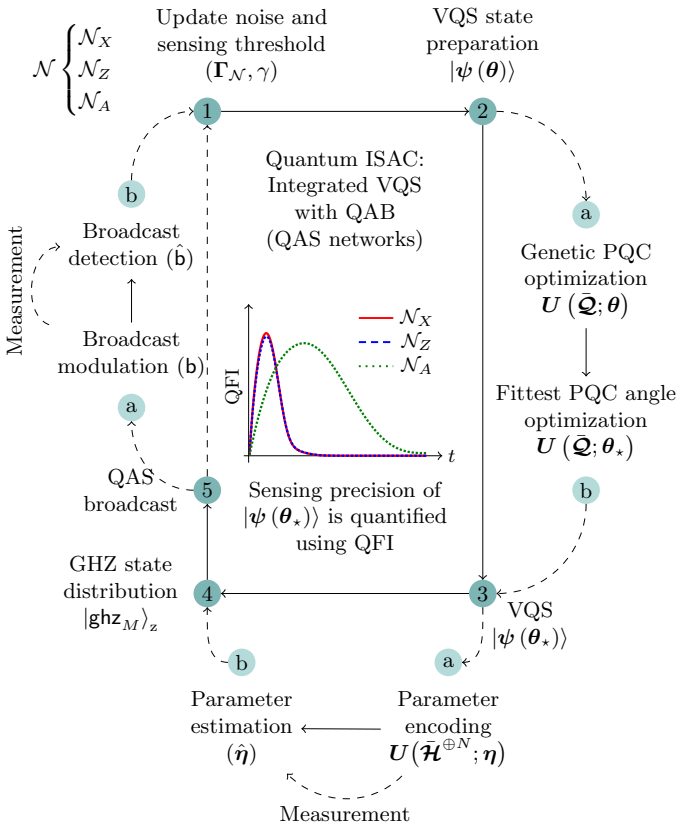

Fig. 1. Quantum anonymous ISAC in a variational and untraceable manner by integrating genetic VQS with QAB. The genetic VQS prepares a high-quality sensing probe state by variationally and evolutionarily finding the tailored PQC structure under quantum noise $\mathcal{N}$. The fittest parameters of the tailored PQC are optimized using classical optimization routines. This genetic VQS probe state now interacts with the physical quantity of interest, which is then estimated by quantum measurement. The sensing information is then anonymously shared with other sensing nodes in the network using the QAB protocol. The protocol starts by distributing the GHZ state (broadcast carrier) among the network participants, followed by the broadcast modulation. The QAS broadcast is then recovered by measurements of all network parties. Here, the noisy maps $\mathcal{N}_X$, $\mathcal{N}_Z$, and $\mathcal{N}_A$ stand for bit-flip, dephasing, and amplitude-damping noises, respectively.

(separable) states.
- We integrate the QAB protocol into VQS networks to anonymously share sensing information among network sensors—ensuring *anonymity* and *untraceability* of sensing data. This QAS broadcast takes a series of steps—i.e., i) broadcast-carrier preparation (GHZ distribution); ii) broadcast modulation (Hadamard and conditional bit-flip operations); iii) broadcast demodulation (computational basis measurement and classical announcement); and iv) broadcast decision (modulo sum calculation).
- We derive the broadcast bit error probability (BEP) for the QAB protocol under anisotropic quantum noise. We show that this QAS broadcast is *error-free*, i.e., zero-BEP under the bit-flip noise, while its BEP under both dephasing and amplitude-damping noises linearly scales with the noise parameter and the number of network sensors in the *low-noise* regime.

The remainder of this paper is organized as follows. Section II preliminarily introduces quantum sensing, including its fundamental limits, Section III briefly reviews the VQAs, and Section IV formally provides the VQS framework. Section V develops the integrated framework of genetic VQS and QAB for QAS networks in noisy environments. Finally, Section VI concludes the paper with a brief summary. In the Appendix, we give the derivations of the BEP for the QAB protocol under bit-flip, dephasing, and amplitude-damping noises.

II. Quantum Sensing

A. Quantum Sensing Frameworks

Generally, quantum sensing follows a series of steps: probe preparation, probe interaction, probe measurement, and estimation.

1) *Probe Preparation:* In the first step, an initial state $|\psi_0\rangle$ of the sensing protocol is evolved by a specific operator to prepare the quantum sensor in a suitable quantum state for interaction with a system of interest. This initial state $|\psi_0\rangle$ is typically set to a known quantum state, such as $|\psi_0\rangle = |0\rangle$. Using a preparation operator $\boldsymbol{W}$, the initial state is prepared in a probe state $|\psi\rangle = \boldsymbol{W}|\psi_0\rangle$ for the sensing purpose.
2) *Probe Interaction:* Using the prepared probe state $|\psi\rangle$, sensing is performed by interacting with a system characterized by a Hamiltonian $\boldsymbol{\mathcal{H}}$. Let η be the physical quantity to be sensed. This quantity is encoded in the system by the unitary operation $\boldsymbol{U}(\boldsymbol{\mathcal{H}};\eta)$, acting on the probe state as follows:
$$\begin{aligned}|\psi(\eta)\rangle &= \boldsymbol{U}(\boldsymbol{\mathcal{H}};\eta)|\psi\rangle \\ &= \exp(-\imath\boldsymbol{\mathcal{H}}\eta)|\psi\rangle\end{aligned} \tag{1}$$
where $\imath = \sqrt{-1}$.
3) *Probe Measurement:* To extract information about the sensing quantity η, the interacted probe state $|\psi(\eta)\rangle$ is measured. The measurement can be done in any basis. Let $\{|\phi_i\rangle\}$ be the measurement basis. Then, this basis can be transformed by applying the unitary operator $\boldsymbol{V}$ to get a different measurement basis $\{\boldsymbol{V}|\phi_i\rangle\}$.
4) *Estimation:* The final step of the protocol involves estimating the unknown quantity η using the measurement outcome μ, based on which measurement vector $\boldsymbol{V}|\phi_i\rangle$ detects the evolved state $|\psi(\eta)\rangle$. Hence, the estimate is generally a function of the measurement outcome as $\hat{\eta}(\mu)$.

Due to the probabilistic nature of quantum measurements, repetitions of sensing are performed to increase the estimation precision. These repetitions can be done in parallel to save the protocol's running time.

B. Quantum Limits

The precision of the estimator $\hat{\eta}$ depends on the sensitivity of the probe state $|\psi\rangle$ on η encoded by the unitary operation $\boldsymbol{U}(\boldsymbol{\mathcal{H}};\eta)$. This sensitivity can be quantified with the QFI, which is a generalization of Fisher information in classical to the quantum regime by maximizing the Fisher information among all possible quantum measurement settings. The QFI is originally defined by a logarithmic derivative operator $\boldsymbol{\mathcal{L}}$ for a quantum state (a density matrix in general) $\boldsymbol{\rho}(\eta)$ as follows:
$$\Xi(\boldsymbol{\rho}(\eta)) = \mathrm{tr}\left[\boldsymbol{\Lambda}^2\boldsymbol{\rho}(\eta)\right] \tag{2}$$
where $\mathrm{tr}(\cdot)$ is the trace operator, $\boldsymbol{\Lambda}$ is implicitly defined as
$$\frac{\partial\boldsymbol{\rho}(\eta)}{\partial\eta} = \frac{1}{2}\{\boldsymbol{\Lambda},\boldsymbol{\rho}(\eta)\}, \tag{3}$$
and $\{\boldsymbol{A},\boldsymbol{B}\} = \boldsymbol{AB}+\boldsymbol{BA}$ is the anti-commutator. Note that the operator $\boldsymbol{\Lambda}$ is called the symmetric logarithmic derivative due to the non-commuting behavior of operators in the quantum state space.

Let $\mathcal{F}(\boldsymbol{\rho},\boldsymbol{\sigma})$ be the Uhlmann fidelity between two quantum states $\boldsymbol{\rho}$ and $\boldsymbol{\sigma}$:
$$\mathcal{F}(\boldsymbol{\rho},\boldsymbol{\sigma}) = \left(\mathrm{tr}\sqrt{\sqrt{\boldsymbol{\rho}}\boldsymbol{\sigma}\sqrt{\boldsymbol{\rho}}}\right)^2, \tag{4}$$
which simplifies to the pure-state fidelity $\mathcal{F}(\psi,\phi) = |\langle\psi|\phi\rangle|^2$ when both $\boldsymbol{\rho}$ and $\boldsymbol{\sigma}$ are pure states, i.e., rank-1 projectors onto state vectors $|\psi\rangle$ and $|\phi\rangle$. The sensitivity of the probe state $|\psi\rangle$ with the parameterized evolution state $|\psi(\eta)\rangle$ is related to the fidelity $|\langle\psi|\psi(\eta)\rangle|^2$ as follows [42]:
$$\Xi(\psi) = \lim_{\eta\to 0} 8\left(\frac{1-\sqrt{\mathcal{F}(\psi,\psi(\eta))}}{\eta^2}\right) \tag{5}$$
where the QFI only depends on the probe state $|\psi\rangle$. For the parameterized evolution in (1) generated by the Hamiltonian $\boldsymbol{\mathcal{H}}$, the QFI can be expressed by the variance of this Hamiltonian as follows:
$$\Xi(\psi) = 4\left(\langle\psi|\boldsymbol{\mathcal{H}}^2|\psi\rangle - \langle\psi|\boldsymbol{\mathcal{H}}|\psi\rangle^2\right). \tag{6}$$
With N-qubit unbiased estimates $\hat{\eta}$, the precision of estimating η is bounded by the QCRB, i.e., the so-called SQL as follows:
$$\mathrm{Var}[\hat{\eta}] \geq \frac{1}{N\Xi(\psi)} \tag{7}$$
where $\mathrm{Var}[\hat{\eta}]$ is the variance of $\hat{\eta}$.

Quantum metrology aims to improve the estimation precision that beats the SQL by leveraging quantum properties

such as entanglement. Let $\lambda_{\max}$ and $\lambda_{\min}$ be the maximum and minimum eigenvalues of the Hamiltonian $\boldsymbol{\mathcal{H}}$, respectively. Note from (6) and considering the Hamiltonian in its eigenvector basis that the QFI is maximized when the measurement outcomes are $\lambda_{\max}$ and $\lambda_{\min}$ with equal probability. Hence, the probe state $|\psi\rangle$ is in an equal superposition of the extreme eigenstates, namely,

$$|\psi\rangle = \frac{|\lambda_{\max}\rangle + |\lambda_{\min}\rangle}{\sqrt{2}}. \tag{8}$$

For N-qubit estimation, the Hamiltonian governing the full system is $\boldsymbol{\mathcal{H}}^{\oplus N}$ where $\oplus$ denotes the Kronecker sum.[1] Hence, the maximum and minimum eigenvalues of this full Hamiltonian are equal to $N\lambda_{\max}$ and $N\lambda_{\min}$ corresponding to the extreme eigenvectors $|\lambda_{\max}\rangle^{\otimes N}$ and $|\lambda_{\min}\rangle^{\otimes N}$, respectively. To maximize the variance of the total Hamiltonian $\boldsymbol{\mathcal{H}}^{\oplus N}$, the N-qubit probe state $|\boldsymbol{\psi}\rangle$ should be prepared as follows:

$$|\boldsymbol{\psi}\rangle = \frac{1}{\sqrt{2}}\left(|\lambda_{\max}\rangle^{\otimes N} + |\lambda_{\min}\rangle^{\otimes N}\right), \tag{9}$$

which is an *entangled* state. Using this entangled state, the estimation precision scales as the Heisenberg limit

$$\mathrm{Var}\left[\hat{\eta}\right] \geq \frac{1}{N^2 \Xi\left(\psi\right)}. \tag{10}$$

Hence, the SQL can be surpassed with quantum resources such as entanglement.

C. Multiparameter Sensing

The extension toward multiparameter quantum sensing is not straightforward from a single parameter due to the non-commuting property of quantum operators, which can cause incompatibility among the measurement operators for each parameter. This incompatibility results in an intricate trade-off in simultaneously extracting information from multiple parameters. Let $\boldsymbol{\eta} = (\eta_1, \eta_2, \ldots, \eta_K)$ be multiple unknown parameters. Then, these K parameters are encoded using the Hamiltonian $\bar{\boldsymbol{\mathcal{H}}} = (\boldsymbol{\mathcal{H}}_1, \boldsymbol{\mathcal{H}}_2, \ldots, \boldsymbol{\mathcal{H}}_K)$ in a unitary operator

$$\boldsymbol{U}\left(\bar{\boldsymbol{\mathcal{H}}}; \boldsymbol{\eta}\right) = \exp\left(-\sum_{k=1}^{K} \imath \boldsymbol{\mathcal{H}}_k \eta_k\right) \tag{11}$$

where $\boldsymbol{\mathcal{H}}_k$ is the Hamiltonian that encodes the kth parameter η_k. In a multiparameter case, the (i,j)th element of the QFI matrix (QFIM) $\boldsymbol{\Xi}\left(\boldsymbol{\rho}\left(\boldsymbol{\eta}\right)\right)$ is defined by [43]

$$\Xi_{ij}\left(\boldsymbol{\rho}\left(\boldsymbol{\eta}\right)\right) = \frac{1}{2}\,\mathrm{tr}\left(\boldsymbol{\rho}\left(\boldsymbol{\eta}\right)\left\{\boldsymbol{\Lambda}_i, \boldsymbol{\Lambda}_j\right\}\right) \tag{12}$$

where the operator $\boldsymbol{\Lambda}_i$ is the symmetric logarithmic derivative for the parameter η_i, defined as

$$\frac{\partial \boldsymbol{\rho}\left(\boldsymbol{\eta}\right)}{\partial \eta_i} = \frac{1}{2}\left\{\boldsymbol{\Lambda}_i, \boldsymbol{\rho}\left(\boldsymbol{\eta}\right)\right\}. \tag{13}$$

[1]For two matrices (operators) $\boldsymbol{A}$ and $\boldsymbol{B}$ of $m \times m$ and $n \times n$, the Kronecker sum is defined as $\boldsymbol{A} \oplus \boldsymbol{B} = \boldsymbol{A} \otimes \boldsymbol{I}_n + \boldsymbol{I}_m \otimes \boldsymbol{B}$, where $\otimes$ denotes the tensor operator and $\boldsymbol{I}_n$ is the $n \times n$ identity operator. We denote $\boldsymbol{I}_2$ simply by $\boldsymbol{I}$ for the qubit case.

For the probe state $|\psi\rangle$, the (i,j)th element of the QFIM $\boldsymbol{\Xi}\left(\psi\right)$ is given by [43]

$$\Xi_{ij}\left(\psi\right) = 2\left\langle\psi\right|\left\{\boldsymbol{\mathcal{H}}_i, \boldsymbol{\mathcal{H}}_j\right\}\left|\psi\right\rangle - 4\left\langle\psi\right|\boldsymbol{\mathcal{H}}_i\left|\psi\right\rangle\left\langle\psi\right|\boldsymbol{\mathcal{H}}_j\left|\psi\right\rangle, \tag{14}$$

which again depends only on the probe state $|\psi\rangle$. The QFIM relates with the fidelity as follows [44]:

$$\boldsymbol{\eta}\boldsymbol{\Xi}\left(\psi\right)\boldsymbol{\eta}^T \approx 8\|\boldsymbol{\eta}\|^2\left(\frac{1 - \sqrt{\mathcal{F}\left(\psi, \psi\left(\epsilon\boldsymbol{\eta}/\|\boldsymbol{\eta}\|\right)\right)}}{\epsilon^2}\right) \tag{15}$$

where T is the transpose operator and $\epsilon \ll 1$ is a small number. Using the QFIM, the precision of the unbiased estimator $\hat{\boldsymbol{\eta}}$ is bounded by

$$\mathrm{Cov}\left[\hat{\boldsymbol{\eta}}\right] \geq \boldsymbol{\Xi}^{-1}\left(\psi\right) \tag{16}$$

where $\mathrm{Cov}\left[\hat{\boldsymbol{\eta}}\right]$ is the covariance matrix of $\hat{\boldsymbol{\eta}}$. Hence, the total variance is bounded by the QCRB as follows:

$$\sum_{k=1}^{K} \mathrm{Var}\left[\hat{\eta}_k\right] \geq \mathrm{tr}\left[\boldsymbol{\Xi}^{-1}\left(\psi\right)\right]. \tag{17}$$

III. Variational Quantum Algorithms

VQAs have emerged as potential solutions for tackling a range of problems using currently available quantum devices. The VQAs are iterative heuristic algorithms that combine quantum and classical computing to find a high-quality solution for a problem of interest. Quantum computing is used to produce a trial solution, while classical computing is used to guide the quantum computer to generate a better solution. Generally, the VQAs consist of three main parts, namely, the PQC, cost function, and classical optimizer.

A. Parameterized Quantum Circuits

A PQC, often called a variational quantum circuit or ansatz, is a distinct class of quantum circuits with adjustable parameters to be tuned using an optimization algorithm by means of a cost function. The design of PQCs can be inspired by insights from a problem of interest. However, in case of an information lack about the problem at hand, the PQC architecture is designed to be more universal.

The PQC generally consists of a series of L unitary operations as follows:

$$\boldsymbol{U}\left(\bar{\boldsymbol{\mathcal{Q}}}; \boldsymbol{\theta}\right) = \boldsymbol{U}\left(\boldsymbol{\mathcal{Q}}_L; \theta_L\right)\cdots\boldsymbol{U}\left(\boldsymbol{\mathcal{Q}}_2; \theta_2\right)\boldsymbol{U}\left(\boldsymbol{\mathcal{Q}}_1; \theta_1\right) \tag{18}$$

where $\boldsymbol{\theta} = (\theta_1, \theta_2, \ldots, \theta_L)$ is the parameter vector to be optimized, $\bar{\boldsymbol{\mathcal{Q}}} = (\boldsymbol{\mathcal{Q}}_1, \boldsymbol{\mathcal{Q}}_2, \ldots, \boldsymbol{\mathcal{Q}}_L)$, and $\boldsymbol{\mathcal{Q}}_\ell$ is the Hamiltonian that encodes the ℓth parameter θ_ℓ for the PQC. Typically, $\boldsymbol{U}\left(\boldsymbol{\mathcal{Q}}_\ell; \theta_\ell\right)$ is local unitary or controlled unitary. The controlled unitary operators are applied to introduce entanglement within the system. On top of a controlled one, unitary operators with interacting Hamiltonians can also produce entanglement. The PQC is required to have the ability to generate a diverse set of quantum states in order to explore various potential solutions. Furthermore, this quantum circuit requires sufficient entanglement generation and manipulation capability to produce more intricate entanglement within the system.

B. Cost Functions

The quality of a trial solution generated by the PQC using the trainable parameters $\boldsymbol{\theta}$ is evaluated through a cost function. Typically, the cost function can be written in the form of

$$C(\boldsymbol{\theta}) = f\left(\{|\phi_i\rangle\}, |\boldsymbol{\psi}(\boldsymbol{\theta})\rangle\right) \tag{19}$$

where f is a real-valued function and $|\boldsymbol{\psi}(\boldsymbol{\theta})\rangle$ is the trial state generated by the PQC. This cost function relies highly on the problem at hand and needs to be trainable in a classical computer. Minimizing the cost function corresponds to optimizing the trial solution, or the optimal cost function corresponds to the best solution for the problem. As the number of parameters increases, the landscape of the cost function becomes more complicated, requiring a good classical optimizer to find a high-quality solution.

C. Classical Optimizers

Navigating the landscape of the cost function to avoid local minima and converge to global optima by tuning the trainable parameters $\boldsymbol{\theta}$ is the main task for the classical optimizer, making it a core component for VQAs. The optimizer seeks to find the optimal parameter

$$\boldsymbol{\theta}_\star = \arg\min C(\boldsymbol{\theta}) \tag{20}$$

by minimizing the cost function. As the number of parameters increases, the number of local minima can also increase, which leads to the optimizer being trapped at this local minima [45]. The ability of the optimizer to avoid these local traps is crucial for finding a good potential solution for the problem at hand.

A gradient-based or -free optimizer can be used to train the parameters of VQAs. The gradient method uses the gradient to guide the optimizer to update the parameter in the direction to minimize the cost function. Typically, in VQAs, the gradient is obtained by the parameter-shift rule that computes the partial derivatives $\partial C/\partial\theta_i$ [46]. The common gradient methods used in VQAs are stochastic gradient descent and Adam optimizer [47], [48]. The gradient optimizer is prone to be trapped at local minima and regions where the gradient of the cost function is flat, hindering its ability to find the global minima [49]. To tackle this issue, gradient-free optimizers are used, such as the constrained optimization by linear approximations (COBYLA), Broyden-Fletcher-Goldfarb-Shanno (BFGS), and evolutionary algorithms [50], [51].

IV. Variational Quantum Sensing

In line with VQAs, the VQS begins by choosing a PQC. This PQC is designed to adaptively learn the optimal settings for both the probe preparation and measurement operators.

A. Single-parameter Sensing

Note from (9) that the optimal probe state is in the entangled form of an equal superposition of two orthogonal states, where all the subsystems for each state are in the same exact state.

1) Probe Preparation: The VQS protocol starts with N qubits all initialized to $|0\rangle$, i.e., the N-qubit state in $|0\rangle^{\otimes N}$. Let $\boldsymbol{H} = (\boldsymbol{\sigma}_{\mathrm{x}} + \boldsymbol{\sigma}_{\mathrm{z}})/\sqrt{2}$ be the Hadamard operator where $\boldsymbol{\sigma}_{\mathrm{x}} = |0\rangle\langle 1| + |1\rangle\langle 0|$ and $\boldsymbol{\sigma}_{\mathrm{z}} = |0\rangle\langle 0| - |1\rangle\langle 1|$ are the Pauli-x and -z operators, respectively. Then, by applying the Hadamard gate $\boldsymbol{H}$ to the first qubit and then sequentially performing controlled-NOT (CNOT) or controlled-$\boldsymbol{\sigma}_{\mathrm{x}}$ gates between the first qubit (control) and all successive qubits (target), the initial state $|\boldsymbol{\psi}_0\rangle$ of the N-qubit sensing system is prepared in the N-partite (maximally entangled) GHZ state as follows:

$$\begin{aligned} |\boldsymbol{\psi}_0\rangle &= \boldsymbol{G}_N \cdots \boldsymbol{G}_2 \boldsymbol{G}_1 |0\rangle^{\otimes N} \\ &= \frac{1}{\sqrt{2}}\left(|0\rangle^{\otimes N} + |1\rangle^{\otimes N}\right) \end{aligned} \tag{21}$$

where

$$\boldsymbol{G}_1 = \boldsymbol{H} \otimes \boldsymbol{I}^{\otimes(N-1)} \tag{22}$$

$$\boldsymbol{G}_i = |0\rangle\langle 0| \otimes \boldsymbol{I}^{\otimes(N-1)} + |1\rangle\langle 1| \otimes \tilde{\boldsymbol{X}}_{i,N} \tag{23}$$

with the Pauli operator $\boldsymbol{\sigma}_{\mathrm{x}}$ acting on the ith qubit

$$\tilde{\boldsymbol{X}}_{i,N} = \boldsymbol{I}^{\otimes(i-2)} \otimes \boldsymbol{\sigma}_{\mathrm{x}} \otimes \boldsymbol{I}^{\otimes(N-i)} \tag{24}$$

for $i = 2, 3, \ldots, N$. After preparing the initial GHZ state $|\boldsymbol{\psi}_0\rangle$, a unitary preparation operator for the basis change can be parameterized such as $\boldsymbol{W}_{\boldsymbol{\theta}} = \boldsymbol{U}\left(\bar{\boldsymbol{\mathcal{Q}}}; \boldsymbol{\theta}\right)$ to obtain the trial probe state $|\boldsymbol{\psi}(\boldsymbol{\theta})\rangle = \boldsymbol{W}_{\boldsymbol{\theta}}|\boldsymbol{\psi}_0\rangle$, where $\boldsymbol{\theta}$ is the parameters to be optimized for probe state preparation. Since the entanglement structure of the optimal probe state is embedded in the initial state $|\boldsymbol{\psi}_0\rangle$, the PQC for the preparation operator $\boldsymbol{W}_{\boldsymbol{\theta}}$ can be designed by only local parameterized unitary operations.

2) Probe Interaction: The trial probe state $|\boldsymbol{\psi}(\boldsymbol{\theta})\rangle$ interacts with the unknown parameter η through the unitary operation $\boldsymbol{U}\left(\boldsymbol{\mathcal{H}}^{\oplus N}; \eta\right)$ to create the state

$$|\boldsymbol{\psi}(\boldsymbol{\theta}; \eta)\rangle = \boldsymbol{U}\left(\boldsymbol{\mathcal{H}}^{\oplus N}; \eta\right)|\boldsymbol{\psi}(\boldsymbol{\theta})\rangle. \tag{25}$$

This interaction state is then measured by the measurement operator. Using the measurement outcomes, the parameter vector $\boldsymbol{\theta}$ is updated to minimize a cost function $C(\boldsymbol{\theta}; \eta)$. Note that the cost function $C(\boldsymbol{\theta}; \eta)$ quantifies how good the trial probe state $|\boldsymbol{\psi}(\boldsymbol{\theta})\rangle$ in estimating the unknown parameter η, which can be done by using the QFI in (5). To maximize the QFI, we utilize the fidelity as the cost function as follows:

$$C(\boldsymbol{\theta}; \eta) = \left|\langle \boldsymbol{\psi}(\boldsymbol{\theta})|\boldsymbol{\psi}(\boldsymbol{\theta}; \eta)\rangle\right|^2. \tag{26}$$

Hence, we need to compute the probability of the interaction state $|\boldsymbol{\psi}(\boldsymbol{\theta}; \eta)\rangle$ collapses to the trial probe state $|\boldsymbol{\psi}(\boldsymbol{\theta})\rangle$ for learning the PQC.

3) Probe Measurement: Since the VQS system is initialized in the computational basis, the unitary operator $\boldsymbol{V}_{\boldsymbol{\theta}}$ for the change of measurement basis can be obtained by the inverse operation of preparing the trial probe state $|\boldsymbol{\psi}(\boldsymbol{\theta})\rangle$ from the state $|0\rangle^{\otimes N}$ as follows:

$$\boldsymbol{V}_{\boldsymbol{\theta}}^{\dagger} = \boldsymbol{W}_{\boldsymbol{\theta}} \boldsymbol{G}_N \cdots \boldsymbol{G}_2 \boldsymbol{G}_1 \tag{27}$$

where $\dagger$ denotes the conjugate transpose. Now, the cost function can be written as

$$C(\boldsymbol{\theta}; \eta) = \left|\langle 0|^{\otimes N} |\boldsymbol{\zeta}(\boldsymbol{\theta}; \eta)\rangle\right|^2 \tag{28}$$

where

$$|\boldsymbol{\zeta}(\boldsymbol{\theta};\eta)\rangle = \boldsymbol{V}_{\boldsymbol{\theta}}\boldsymbol{U}\big(\boldsymbol{\mathcal{H}}^{\oplus N};\eta\big)\boldsymbol{V}_{\boldsymbol{\theta}}^{\dagger}\,|0\rangle^{\otimes N} \tag{29}$$

is the PQC output state ready for the computational basis measurement. Hence, the cost function $C(\boldsymbol{\theta};\eta)$ can be seen as the probability that the output state $|\boldsymbol{\zeta}(\boldsymbol{\theta};\eta)\rangle$ collapses into the state $|0\rangle^{\otimes N}$.

B. Multiparameter Sensing

In a single-parameter case, the structure of the optimal probe state is analytically known, which guides the design of PQCs. The optimal structure is generally challenging to obtain in a multiparameter case. Hence, we design a more generic PQC to explore a large range of trial solutions.

1) Probe Preparation: To devise a more generic PQC, we consider a local or entangling unitary operator $\boldsymbol{U}(\boldsymbol{\mathcal{Q}}_\ell;\theta_\ell)$. The entangling unitary operator can be in the form of

$$\boldsymbol{U}(\boldsymbol{\mathcal{Q}}_\ell;\theta_\ell) = |0\rangle\langle 0|\otimes\boldsymbol{I} + |1\rangle\langle 1|\otimes\exp(-\imath\boldsymbol{\mathcal{Q}}_\ell\theta_\ell), \tag{30}$$

which is a controlled unitary operator that only performs the local unitary operator $\exp(-\imath\boldsymbol{\mathcal{Q}}_\ell\theta_\ell)$ to the target qubit when the state of the control qubit is in $|1\rangle$ and leave it unchanged, otherwise. Using nonlocal Hamiltonian $\boldsymbol{\mathcal{Q}}_\ell$, another entangling unitary operator is in the form of

$$\boldsymbol{U}(\boldsymbol{\mathcal{Q}}_\ell;\theta_\ell) = \exp(-\imath\boldsymbol{\mathcal{Q}}_\ell\theta_\ell). \tag{31}$$

Let the initial state of the quantum sensor be $|\boldsymbol{\psi}_0\rangle = |0\rangle^{\otimes N}$. Then, the trial probe state is prepared as follows:

$$|\boldsymbol{\psi}(\boldsymbol{\theta})\rangle = \boldsymbol{U}\left(\bar{\boldsymbol{\mathcal{Q}}};\boldsymbol{\theta}\right)|0\rangle^{\otimes N}. \tag{32}$$

2) Probe Interaction: The unknown parameters $\boldsymbol{\eta}$ are encoded by the total Hamiltonian

$$\bar{\boldsymbol{\mathcal{H}}}^{\oplus N} = \left(\boldsymbol{\mathcal{H}}_1^{\oplus N}, \boldsymbol{\mathcal{H}}_2^{\oplus N}, \ldots, \boldsymbol{\mathcal{H}}_K^{\oplus N}\right) \tag{33}$$

in the unitary operator $\boldsymbol{U}\big(\bar{\boldsymbol{\mathcal{H}}}^{\oplus N};\boldsymbol{\eta}\big)$, which then interacts with the trial probe state $|\boldsymbol{\psi}(\boldsymbol{\theta})\rangle$ to generate the state

$$|\boldsymbol{\psi}(\boldsymbol{\theta};\boldsymbol{\eta})\rangle = \boldsymbol{U}\big(\bar{\boldsymbol{\mathcal{H}}}^{\oplus N};\boldsymbol{\eta}\big)\,\boldsymbol{U}\left(\bar{\boldsymbol{\mathcal{Q}}};\boldsymbol{\theta}\right)|0\rangle^{\otimes N}. \tag{34}$$

This multiparameter evolved state is tested by the cost function $C(\boldsymbol{\theta};\boldsymbol{\eta})$ using the quantum measurement outcomes. Following (15), we also use the fidelity between the trial probe state $|\boldsymbol{\psi}(\boldsymbol{\theta})\rangle$ and the generated state $|\boldsymbol{\psi}(\boldsymbol{\theta};\boldsymbol{\eta})\rangle$ as the cost function.

3) Probe Measurement: Since the cost function is the fidelity between the trial probe and generated states, the unitary operator $\boldsymbol{V}_{\boldsymbol{\theta}}$ for the change of measurement basis is simply given by

$$\boldsymbol{V}_{\boldsymbol{\theta}} = \boldsymbol{U}^{\dagger}\left(\bar{\boldsymbol{\mathcal{Q}}};\boldsymbol{\theta}\right). \tag{35}$$

The cost function is then calculated by evolving the generated state $|\boldsymbol{\psi}(\boldsymbol{\theta};\boldsymbol{\eta})\rangle$ using $\boldsymbol{U}\left(\bar{\boldsymbol{\mathcal{Q}}};\boldsymbol{\theta}\right)$ and compute the probability of finding the state $|0\rangle^{\otimes N}$ as follows:

$$C(\boldsymbol{\theta};\boldsymbol{\eta}) = \left|\langle 0|^{\otimes N}\,\boldsymbol{U}^{\dagger}\left(\bar{\boldsymbol{\mathcal{Q}}};\boldsymbol{\theta}\right)|\boldsymbol{\psi}(\boldsymbol{\theta};\boldsymbol{\eta})\rangle\right|^2. \tag{36}$$

V. Integrated VQS with QAC

We now consider a QSN of M sensors where each quantum sensor can tailor its quantum state variationally. These sensors employ a *genetic* VQA to variationally prepare the probe state. The PQC is designed by a GA approach for the physical quantity of interest (e.g., magnetic-field sensing for localization or classification). After interacting and estimating the physical quantity, the sensor anonymously broadcasts the sensing information to all network sensors. This framework for QAS networks integrates the genetic VQS with the QAB protocol to ensure anonymity and untraceability.

A. Genetic VQS

Finding a high-quality PQC is hard due to the large PQC space. Herein, we utilize a genetic approach inspired by the process of natural selection to heuristically search the PQC structure for the magnetic-field sensing task.

1) Genetic PQCs: The PQCs used in quantum algorithms highly determine the quality of a probe state obtained by VQS. To find the PQC structure, we employ a GA method to heuristically find the circuit structure [52]. The GA starts by initializing the population that consists of q chromosomes

$$\mathcal{P} = \left\{\mathfrak{p}_1, \mathfrak{p}_2, \ldots, \mathfrak{p}_q\right\}. \tag{37}$$

The ith chromosome $\mathfrak{p}_i$ contains a series of genes as follows:

$$\mathfrak{p}_i = \begin{bmatrix} (\boldsymbol{\mathcal{A}}_{i1}, |c_{i1}\rangle, |t_{i1}\rangle, \theta_{i1}) \\ (\boldsymbol{\mathcal{A}}_{i2}, |c_{i2}\rangle, |t_{i2}\rangle, \theta_{i2}) \\ \vdots \\ (\boldsymbol{\mathcal{A}}_{i\ell_i}, |c_{i\ell_i}\rangle, |t_{i\ell_i}\rangle, \theta_{i\ell_i}) \end{bmatrix} \tag{38}$$

where $\boldsymbol{\mathcal{A}}_{ij}$ is a Hamiltonian taken from a set $\{\boldsymbol{\sigma}_{\mathrm{x}}, \boldsymbol{\sigma}_{\mathrm{y}}, \boldsymbol{\sigma}_{\mathrm{z}}\}$ of Pauli operators, $\boldsymbol{\sigma}_{\mathrm{y}} = \imath\boldsymbol{\sigma}_{\mathrm{x}}\boldsymbol{\sigma}_{\mathrm{z}}$ is the Pauli-y operator, $|c_{ij}\rangle$ is the control qubit, $|t_{ij}\rangle$ is the target qubit, θ_{ij} is the parameter, and ℓ_i is the length of genes. The gene is mapped into a single- or two-qubit unitary operator. For a single-qubit unitary operator, the control qubit $|c_{ij}\rangle$ is not defined, and the unitary operator $\boldsymbol{U}(\boldsymbol{\mathcal{A}}_{ij};\theta_{ij}) = \exp(-\imath\boldsymbol{\mathcal{A}}_{ij}\theta_{ij})$ is applied on the target qubit $|t_{ij}\rangle$. The two-qubit unitary operator is in the controlled unitary form of $\boldsymbol{U}(\boldsymbol{\mathcal{A}}_{ij};\theta_{ij}) = |0\rangle\langle 0|\otimes\boldsymbol{I} + |1\rangle\langle 1|\otimes\exp(-\imath\boldsymbol{\mathcal{A}}_{ij}\theta_{ij})$ and is applied on the control and target qubits $|c_{ij}\rangle\otimes|t_{ij}\rangle$.

All the chromosomes in the population are tested by calculating the QFI for the generated state

$$|\boldsymbol{\psi}(\boldsymbol{\theta})\rangle = \mathcal{M}(\mathfrak{g}_{\ell_i})\cdots\mathcal{M}(\mathfrak{g}_2)\,\mathcal{M}(\mathfrak{g}_1)\,|\boldsymbol{\psi}_0\rangle \tag{39}$$

where $\mathcal{M}$ is the map from the gene to the unitary operator, $\mathfrak{g}_k$ is the kth gene of the chromosome, and $|\boldsymbol{\psi}_0\rangle = |0\rangle^{\otimes N}$. The density matrix $|\boldsymbol{\psi}(\boldsymbol{\theta})\rangle\langle\boldsymbol{\psi}(\boldsymbol{\theta})|$ is evolved using the Lindblad master equation. Based on the corresponding QFI, each chromosome with the best fitness is chosen as a parent for generating the next generation of the population. On top of the best chromosome, the other parents are determined by using tournament selection, where the tournament round and size are set to r and s, making the parents of total $r+1$ chromosomes. These parents are included in the next generation. To generate the offspring, we employ the crossover operation that takes

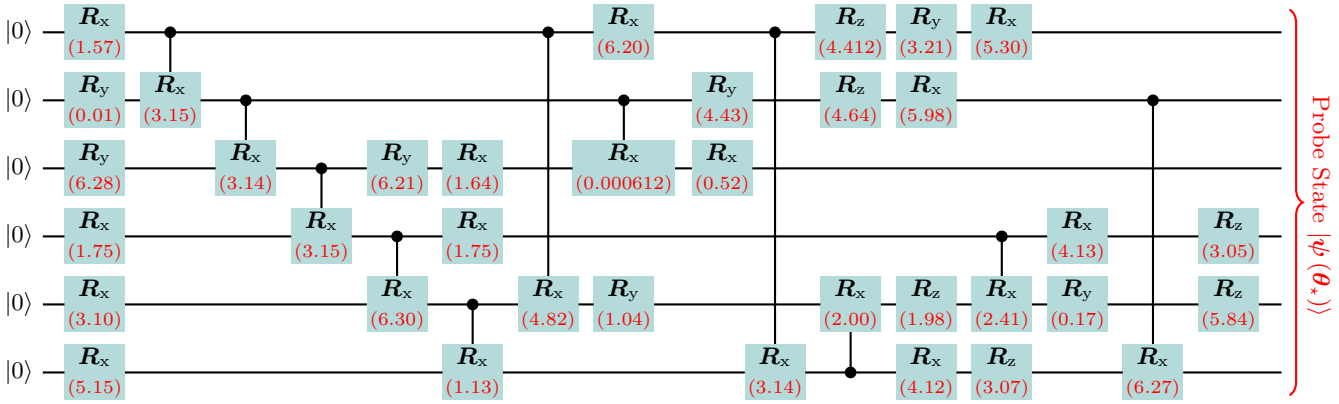

(a) Optimized PQC

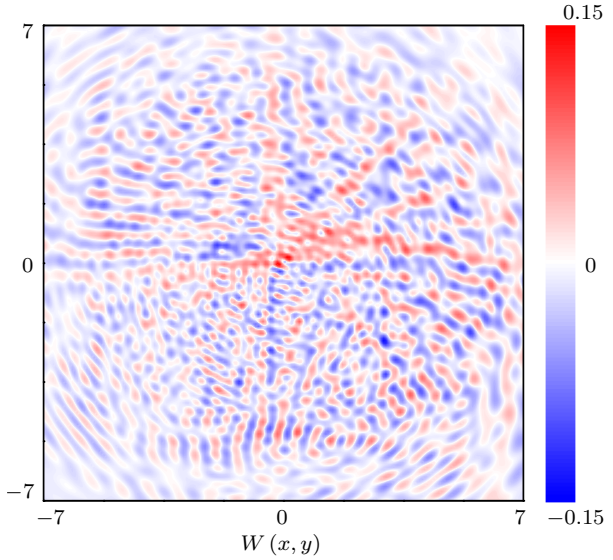

(b) Wigner function

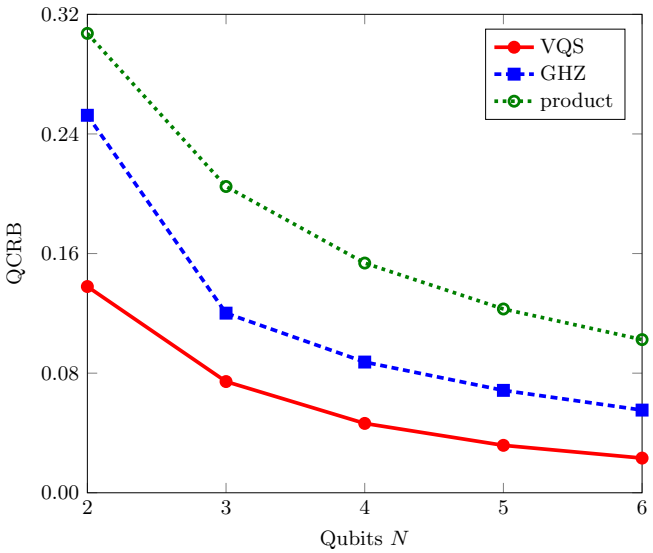

(c) QCRB

Fig. 2. Genetic VQS probe state $|\boldsymbol{\psi}(\boldsymbol{\theta}_\star)\rangle$ for scalar magnetic-field sensing ($N = 6$) under bit-flip noise where the bit-flip noise acts independently on each qubit at the decay rate of $\gamma_i = 0.1$ for all qubits. (a) The PQC structure that maximizes the QFI is obtained by the GA for $N = 6$ where the red values denote the optimized angle parameters. The PQC consists of single-qubit rotation gates $\boldsymbol{R}_{\mathrm{v}}(\theta) = \exp(-\imath\boldsymbol{\sigma}_{\mathrm{v}}\theta/2)$ and two-qubit gates in the form of controlled-$\boldsymbol{R}_{\mathrm{x}}(\theta)$ gates, where $\mathrm{v} \in \{\mathrm{x}, \mathrm{y}, \mathrm{z}\}$ and $\theta \in [0, 2\pi]$. (b) The Wigner function $W(x, y)$ for the optimized VQS probe state $|\boldsymbol{\psi}(\boldsymbol{\theta}_\star)\rangle$ is plotted as a function of phase-space parameters (x, y) using the QuTiP (quantum toolbox in Python) package. (c) The QCRB is plotted for VQS, GHZ, and product states as a function of the number N of qubits involved in the sensing process, where the noisy quantum-state evolution governed by the Lindblad master equation in (42) is also simulated using the QuTiP and the VQS probe state is optimized for each N.

two parents as the input and generates a new chromosome. The crossover operation extracts a sequence of genes with random length from one parent and puts it as the child genes. Then, another sequence of genes with random length from another parent is appended to the child's chromosome. After the child is generated from the crossover operation, the child undergoes a series of mutation operations.

- *Qubit Mutation*: This mutation operator changes the control and target qubits of each gene randomly at a specific mutation probability.
- *Parameter Mutation*: This mutation operator adds the parameter of each gene with a value taken from a zero-mean normal distribution with a chosen standard deviation at a specific mutation probability.
- *Genes Deletion*: This operator randomly removes a series of genes within the chromosome.
- *Genes Insertion*: This operator generates a random series of genes and inserts it randomly in the chromosome.
- *Genes Replacement*: This operator performs gene deletion and insertion operators sequentially.
- *Genes Swaping*: This operator picks two series of genes randomly and swaps them.
- *Genes Permutation*: This operator selects a series of genes randomly and performs random shuffling of the elements of the series.

The next generation then repeats the same procedures for the evaluation, parent selection, crossover operation, and mutation operation with a specific number of iterations.

2) Scalar Magnetic-Field Sensing: For the single-parameter VQS to estimate the amplitude of a magnetic field, we consider that the vector $\boldsymbol{\eta} = (\eta_1, \eta_2, \eta_3)$ of magnetic field components is encoded by the Hamiltonian $\bar{\boldsymbol{\mathcal{H}}} = \frac{1}{2}(\boldsymbol{\sigma}_{\mathrm{x}}, \boldsymbol{\sigma}_{\mathrm{y}}, \boldsymbol{\sigma}_{\mathrm{z}})$ in the

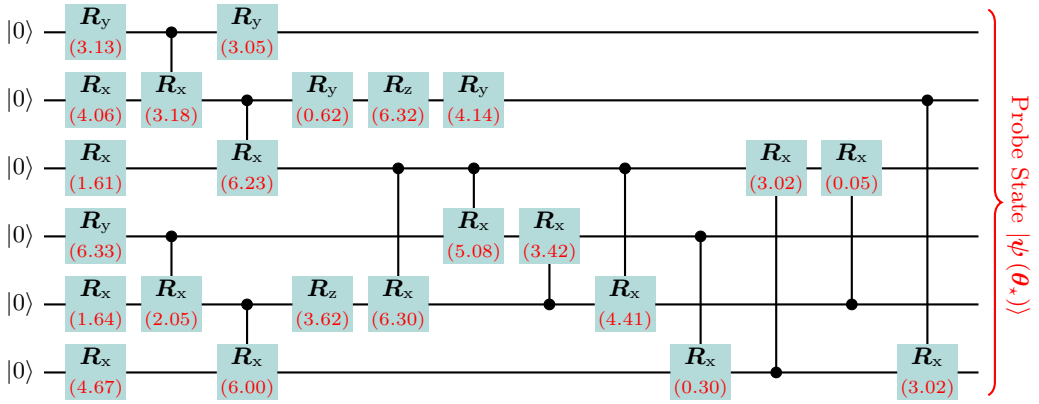

(a) Optimized PQC

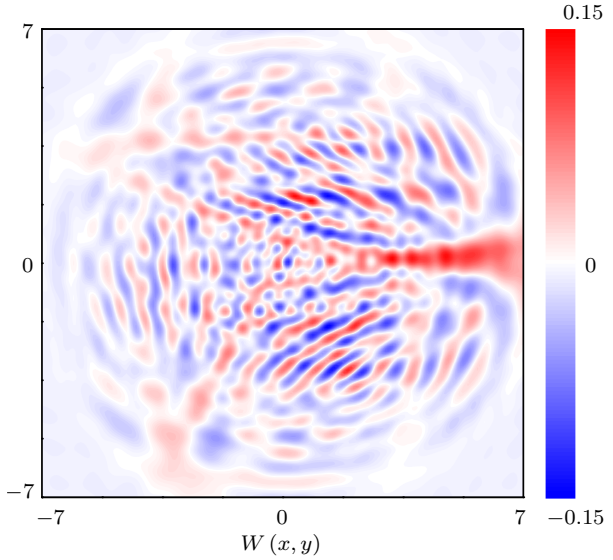

(b) Wigner function

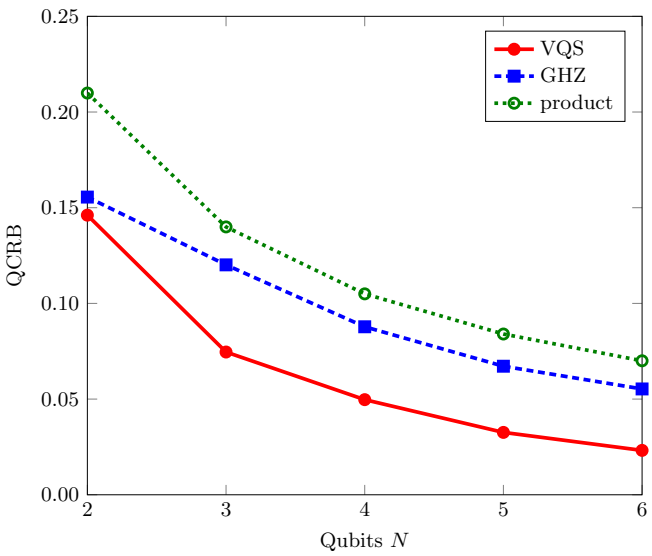

(c) QCRB

Fig. 3. Genetic VQS probe state $|\boldsymbol{\psi}(\boldsymbol{\theta}_\star)\rangle$ for scalar magnetic-field sensing ($N = 6$) under dephasing noise with the same parameters as in Fig. 2.

unitary operator

$$\boldsymbol{U}\left(\bar{\boldsymbol{\mathcal{H}}};\boldsymbol{\eta}\right) = \exp\left[-\frac{\imath}{2}\left(\boldsymbol{\sigma}_{\mathrm{x}}\eta_1 + \boldsymbol{\sigma}_{\mathrm{y}}\eta_2 + \boldsymbol{\sigma}_{\mathrm{z}}\eta_3\right)\right]. \tag{40}$$

To cast it as a single-parameter problem, we rewrite the Hamiltonian of $\boldsymbol{U}\left(\bar{\boldsymbol{\mathcal{H}}};\boldsymbol{\eta}\right)$ as $\boldsymbol{\mathcal{H}} = \left(\boldsymbol{\sigma}_{\mathrm{x}}\eta_1 + \boldsymbol{\sigma}_{\mathrm{y}}\eta_2 + \boldsymbol{\sigma}_{\mathrm{z}}\eta_3\right)/\left(2\|\boldsymbol{\eta}\|\right)$ and the unitary evolution as $\boldsymbol{U}\left(\boldsymbol{\mathcal{H}};\|\boldsymbol{\eta}\|\right) = \exp\left(-\imath\boldsymbol{\mathcal{H}}\|\boldsymbol{\eta}\|\right)$ for VQS to sense the amplitude of the magnetic field $\|\boldsymbol{\eta}\|$.

The eigenvectors of the Hamiltonian $\boldsymbol{\mathcal{H}}$ can be identified by the density matrix form as follows:

$$\begin{aligned}\boldsymbol{\rho}_\lambda &= |\lambda\rangle\langle\lambda| \\ &= \frac{1}{2}\left(\boldsymbol{I} + a_1\boldsymbol{\sigma}_{\mathrm{x}} + a_2\boldsymbol{\sigma}_{\mathrm{y}} + a_3\boldsymbol{\sigma}_{\mathrm{z}}\right)\end{aligned} \tag{41}$$

where $\boldsymbol{a} = (a_1, a_2, a_3) = \boldsymbol{\eta}/\|\boldsymbol{\eta}\|$ for $|\lambda_{\max}\rangle$ and $\boldsymbol{a} = -\boldsymbol{\eta}/\|\boldsymbol{\eta}\|$ for $|\lambda_{\min}\rangle$. Hence, in the noiseless case, the optimal probe state for the N-qubit sensing system can be obtained variationally with a simple local PQC such as $\boldsymbol{U}\left(\bar{\boldsymbol{\mathcal{Q}}};\boldsymbol{\theta}\right) = \boldsymbol{U}\left(\boldsymbol{\sigma}_{\mathrm{x}}^{\oplus N};\boldsymbol{\theta}\right)$ with the initial GHZ state $|\psi_0\rangle$ in (21) to achieve the Heisenberg scaling. When the magnetic field is only in the z-axis direction, i.e., $\boldsymbol{\eta} = (0, 0, \eta_3)$, the GHZ-type and product states have the same precision scaling, and hence we need to obtain a better probe state [35]. In noisy cases, the GHZ-type state may not also be optimal due to its sensitivity to noise. We consider the completely positive trace-preserving (CPTP) evolution of a quantum state in a noisy environment to be governed by the Lindblad master equation

$$\frac{d\boldsymbol{\rho}_\lambda(t)}{dt} = -\imath\left[\boldsymbol{\mathcal{H}}\|\boldsymbol{\eta}\|, \boldsymbol{\rho}_\lambda(t)\right] + \boldsymbol{\mathcal{L}}\left(\boldsymbol{\rho}_\lambda(t)\right) \tag{42}$$

with

$$\boldsymbol{\mathcal{L}}\left(\boldsymbol{\rho}_\lambda(t)\right) = \sum_{i=1}^{N}\gamma_i\left(\boldsymbol{\Gamma}_i\boldsymbol{\rho}_\lambda(t)\boldsymbol{\Gamma}_i^\dagger - \frac{1}{2}\left\{\boldsymbol{\Gamma}_i^\dagger\boldsymbol{\Gamma}_i, \boldsymbol{\rho}_\lambda(t)\right\}\right) \tag{43}$$

where $[\boldsymbol{A}, \boldsymbol{B}] = \boldsymbol{AB} - \boldsymbol{BA}$ is the commutator, γ_i is the decay rate, and $\boldsymbol{\Gamma}_i$ is the decay operator. The first term in the master equation (42) corresponds to the noiseless evolution, whereas the second term $\boldsymbol{\mathcal{L}}\left(\boldsymbol{\rho}_\lambda(t)\right)$ relates to the interaction between the system and environment, generating non-unitary dynamics.

Bit-Flip Quantum Noise: The decay operator $\boldsymbol{\Gamma}_i$ is given by the bit-flip Pauli operator $\boldsymbol{\sigma}_{\mathrm{x}}$ acting on the ith qubit, i.e.,

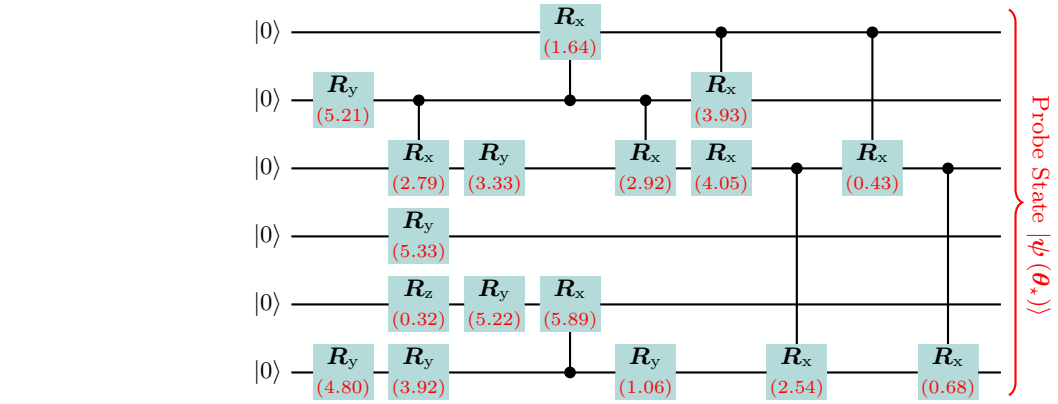

(a) Optimized PQC

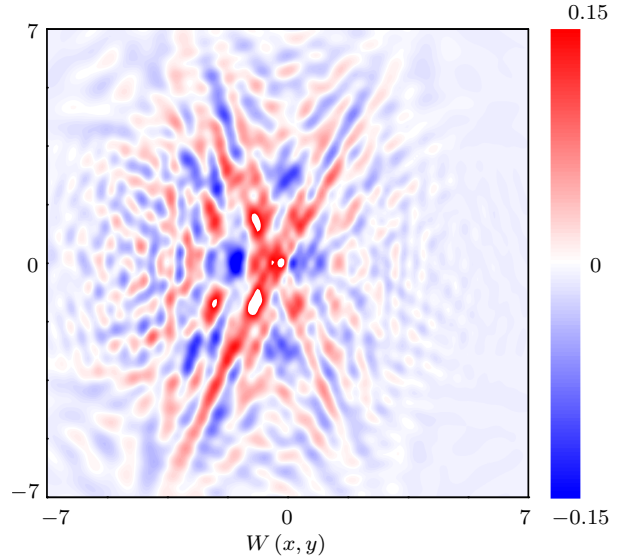

(b) Wigner function

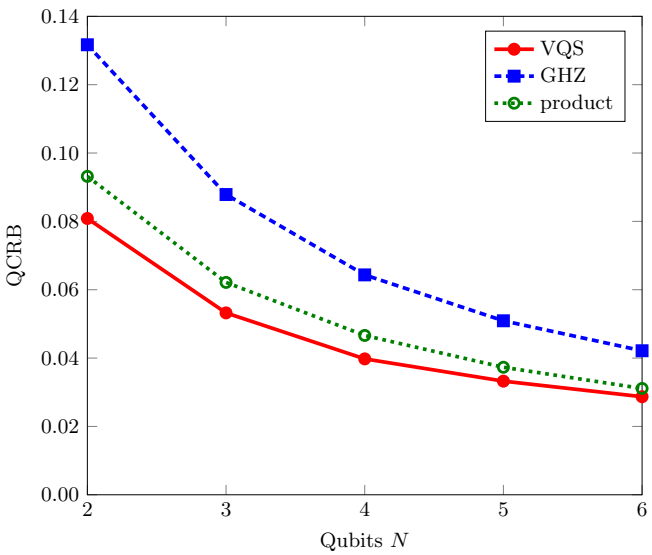

(c) QCRB

Fig. 4. Genetic VQS probe state $|\psi(\boldsymbol{\theta}_\star)\rangle$ for scalar magnetic-field sensing ($N = 6$) under amplitude-damping noise with the same parameters as in Fig. 2.

$\boldsymbol{\Gamma}_i = \boldsymbol{X}_{i,N}$ where

$$\boldsymbol{X}_{i,N} = \boldsymbol{I}^{\otimes(i-1)} \otimes \boldsymbol{\sigma}_{\mathrm{x}} \otimes \boldsymbol{I}^{\otimes(N-i)}. \tag{44}$$

Hence, the non-unitary dynamics $\boldsymbol{\mathcal{L}}(\boldsymbol{\rho}_\lambda(t))$ for the bit-flip noise is given by

$$\boldsymbol{\mathcal{L}}(\boldsymbol{\rho}_\lambda(t)) = \sum_{i=1}^{N} \gamma_i \left(\boldsymbol{X}_{i,N} \boldsymbol{\rho}_\lambda(t) \boldsymbol{X}_{i,N} - \boldsymbol{\rho}_\lambda(t)\right). \tag{45}$$

Dephasing (Phase-Flip) Quantum Noise: The decay operator $\boldsymbol{\Gamma}_i$ is given by the phase-flip Pauli operator $\boldsymbol{\sigma}_{\mathrm{z}}$ acting on the ith qubit, i.e., $\boldsymbol{\Gamma}_i = \boldsymbol{Z}_{i,N}$ where

$$\boldsymbol{Z}_{i,N} = \boldsymbol{I}^{\otimes(i-1)} \otimes \boldsymbol{\sigma}_{\mathrm{z}} \otimes \boldsymbol{I}^{\otimes(N-i)}. \tag{46}$$

The non-unitary dynamics $\boldsymbol{\mathcal{L}}(\boldsymbol{\rho}_\lambda(t))$ for the dephasing noise is then given by

$$\boldsymbol{\mathcal{L}}(\boldsymbol{\rho}_\lambda(t)) = \sum_{i=1}^{N} \gamma_i \left(\boldsymbol{Z}_{i,N} \boldsymbol{\rho}_\lambda(t) \boldsymbol{Z}_{i,N} - \boldsymbol{\rho}_\lambda(t)\right). \tag{47}$$

Amplitude-Damping (Energy-Relaxation) Quantum Noise: The decay operator $\boldsymbol{\Gamma}_i$ is given by the combined Pauli operator $\boldsymbol{\sigma}_{\mathrm{xy}} = (\boldsymbol{\sigma}_{\mathrm{x}} + \imath\boldsymbol{\sigma}_{\mathrm{y}})/2$ acting on the ith qubit as follows:

$$\boldsymbol{\Gamma}_i = \boldsymbol{I}^{\otimes(i-1)} \otimes \boldsymbol{\sigma}_{\mathrm{xy}} \otimes \boldsymbol{I}^{\otimes(N-i)}. \tag{48}$$

Numerical Examples: Figs. 2–4 show the prepared genetic VQS probe states $|\psi(\boldsymbol{\theta}_\star)\rangle$ for scalar magnetic-field sensing when $N = 6$ under bit-flip, dephasing, and amplitude-damping noises, respectively, where the noise acts independently on each qubit at the decay rate of $\gamma_i = 0.1$ for all qubits. The PQC structure that maximizes the QFI is obtained by the GA with 30 chromosomes ($q = 30$), 3 tournament rounds ($r = 3$), and 7 tournament sizes ($s = 7$) for each N. The PQC consists of single-qubit rotation gates $\boldsymbol{R}_{\mathrm{v}}(\theta) = \exp(-\imath\boldsymbol{\sigma}_{\mathrm{v}}\theta/2)$ and two-qubit controlled-$\boldsymbol{R}_{\mathrm{x}}(\theta)$ gates, where $\mathrm{v} \in \{\mathrm{x}, \mathrm{y}, \mathrm{z}\}$ and $\theta \in [0, 2\pi]$. The optimized angle parameters are shown in red values. The Wigner function $W(x, y)$ for the optimized VQS probe state $|\psi(\boldsymbol{\theta}_\star)\rangle$ is plotted as a function of phase-space parameters (x, y). The Wigner function is a quasi-probability distribution function on the position and

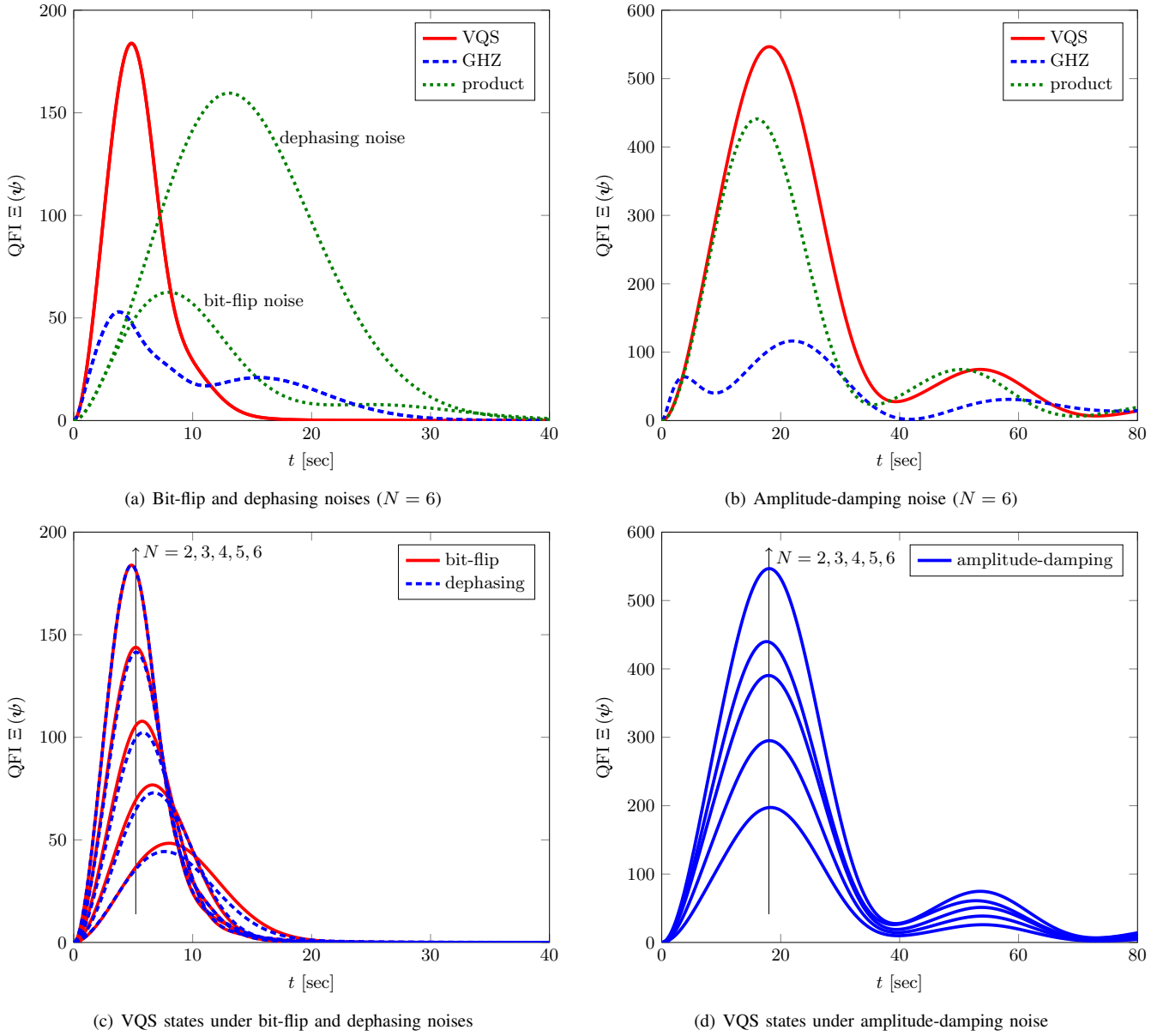

(a) Bit-flip and dephasing noises ($N = 6$)

(b) Amplitude-damping noise ($N = 6$)

(c) VQS states under bit-flip and dephasing noises

(d) VQS states under amplitude-damping noise

Fig. 5. QFI $\Xi(\boldsymbol{\psi})$ for scalar magnetic-field sensing as a function of t seconds under quantum noise as in Figs. 2–4. The QFI for VQS, GHZ, and product probe states is plotted under (a) bit-flip and dephasing noises and (b) amplitude-damping noise when $N = 6$. In addition, the QFI for the VQS probe state is plotted under (c) bit-flip and dephasing noises and (d) amplitude-damping noise when $N = 2, 3, 4, 5$, and 6.

momentum variables and is defined for the density matrix $\boldsymbol{\rho}$ as

$$W(x,y) = \frac{1}{\pi\hbar}\int_{-\infty}^{\infty} \langle x-\tau|\,\boldsymbol{\rho}\,|x+\tau\rangle\, e^{2\imath y\tau/\hbar} d\tau \qquad (49)$$

where $\hbar$ is the reduced Planck's constant. This function is useful to characterize non-classical quantum states by visualizing quantum phenomena such as squeezing and entanglement with their negative values [53]. Hence, the Wigner function shows that the tailored VQS probe states $|\boldsymbol{\psi}(\boldsymbol{\theta}_\star)\rangle$ are non-classical as indicated by their negative values. We also compare the QCRB for VQS, GHZ, and product states when $N = 2, 3, 4, 5$, and 6, where the noisy quantum-state evolution governed by the Lindblad master equation in (42). We can see from the figures that VQS probe states exhibit improved precision bounds for all three types of quantum noise. Both GHZ and product states are in the eigenbasis of the Hamiltonian $\boldsymbol{\mathcal{H}}$. It can be seen that the GHZ and product states are more prone to the bit-flip and dephasing noises as compared to the amplitude-damping noise. However, the product state is more robust to the dephasing noise than the bit-flip noise and outperforms the GHZ for the amplitude-damping case. The VQS state is also more prone to the bit-flip and dephasing noises than the amplitude-damping noise when $N = 2, 3$, and 4. The VQS state is tailored to have roughly similar precision bounds for all three noises.

Fig. 5 shows the QFI $\Xi(\boldsymbol{\psi})$ for scalar magnetic-field sensing as a function of t seconds under quantum noise as in Figs. 2–4. The maximum value of QFI represents the fundamental sensitivity the quantum state can achieve. The required time to reach this value is also valuable in quantum sensing, especially

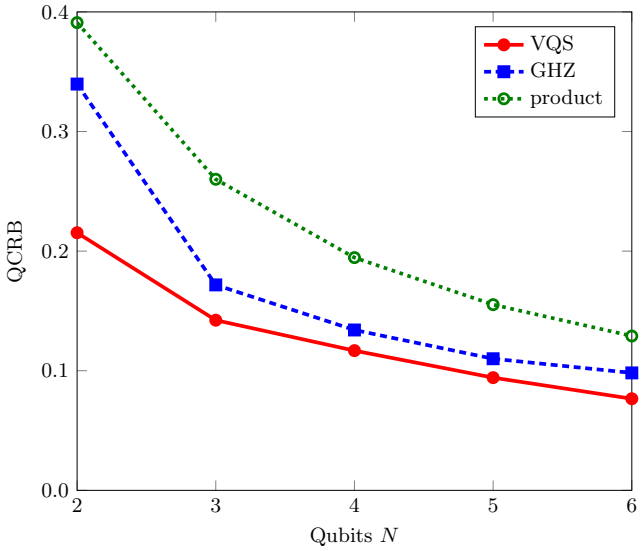

Fig. 6. QCRBs for vector magnetic-field sensing with VQS, GHZ, and product probe states as a function of N under bit-flip noise as in Fig. 2(c).

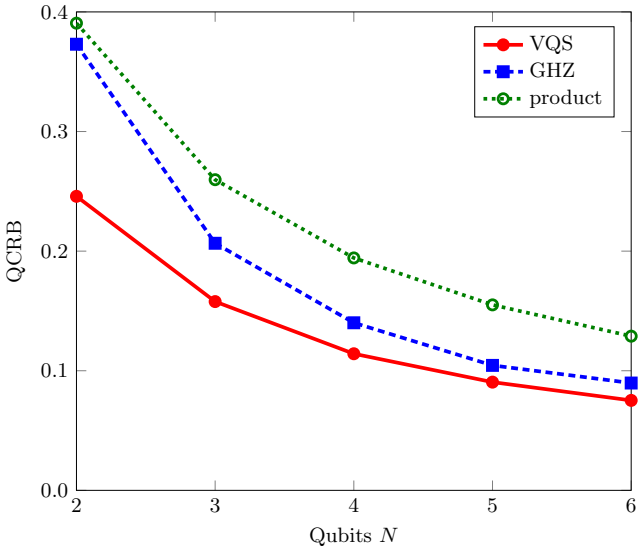

Fig. 7. QCRBs for vector magnetic-field sensing with VQS, GHZ, and product probe states as a function of N under dephasing noise as in Fig. 3(c).

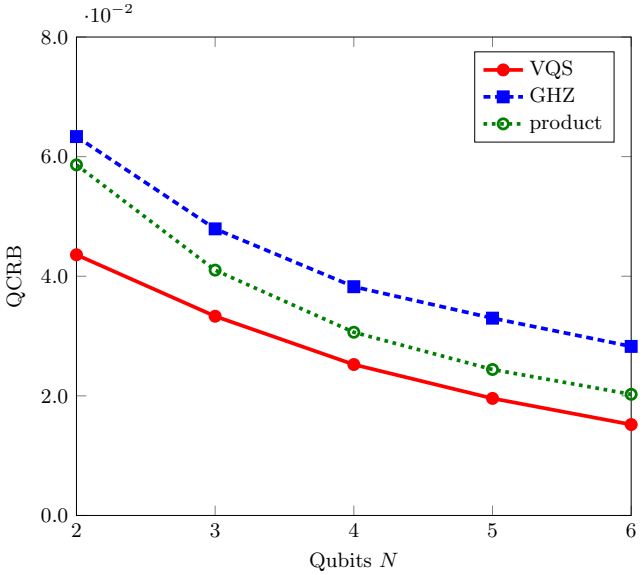

Fig. 8. QCRBs for vector magnetic-field sensing with VQS, GHZ, and product probe states as a function of N under amplitude-damping noise as in Fig. 4(c).

in noisy and time-critical scenarios. Generally, the maximum achievable QFI should be acquired quickly to enable faster, more precise, and more efficient parameter estimation. Therefore, the metrological precision of noisy quantum sensing can be comparatively evaluated by analyzing temporal dynamics of QFI for respective probe states. We can see from Fig. 5(a) and 5(b) that the VQS probe state reaches its larger QFI peak at a negligibly delayed time than the GHZ or product states, as expected. Fig. 5(a) shows a negligible QFI difference for VQS and GHZ states under bit-flip and dephasing noises, while the product probe state peaks at a delayed time with a large value in dephasing noise. The GHZ probe state peaks marginally faster, while the VQS state attains a notably higher maximum QFI. As seen from Fig. 5(b), the time difference to reach QFI peak is negligible, but the maximum values significantly vary in the order of VQS, product, and GHZ probe states under the amplitude damping noise. Figs. 5(c) and 5(d) show the QFI achieved by VQS probe states under bit-flip, dephasing, and amplitude-dampling noises when $N = 2, 3, 4, 5$, and 6. As the number N of qubits increases, the maximum achievable QFI notably increases, while the time to reach its peak decreases slightly under bit-flip and dephasing noises or remains largely unchanged for amplitude-damping noise. We can also see from Fig. 5(c) that the QFI difference under bit-flip and dephasing noise nearly vanishes as N increases.

3) Vector Magnetic-Field Sensing: To sense all the magnetic field components, multiparameter sensing is employed for simultaneous parameter estimation. In contrast to using qubits for individual component estimation, this method leverages all the qubits at once, offering improved precision. The optimal probe state for simultaneously estimating all magnetic field components is not as well established as in the single-parameter case. Using a single- or two-qubit system, the GHZ state is optimal for two-dimensional magnetic-field sensing. However, the GHZ state may not be optimal for larger systems. For the three-dimensional magnetic field, the GHZ state even leads to a singular QFIM for one or two qubits.

Since the Pauli operators $\boldsymbol{\sigma}_{\mathrm{x}}$,$\boldsymbol{\sigma}_{\mathrm{y}}$, and $\boldsymbol{\sigma}_{\mathrm{z}}$ are *traceless* and have -1 *determinant*, the eigenvalues of each Pauli operator are equal to ± 1. Let $|\pm 1\rangle_{\mathrm{v}}$ be the normalized eigenvectors corresponding to eigenvalues ± 1 for the Pauli operator $\boldsymbol{\sigma}_{\mathrm{v}}$ for $\mathrm{v} \in \{\mathrm{x}, \mathrm{y}, \mathrm{z}\}$. The eigenvectors of the Pauli operators $\boldsymbol{\sigma}_{\mathrm{x}}$ and $\boldsymbol{\sigma}_{\mathrm{y}}$ are linear combinations of the eigenvectors of $\boldsymbol{\sigma}_{\mathrm{z}}$ and $\boldsymbol{\sigma}_{\mathrm{x}}$, respectively, as follows:

$$|\pm 1\rangle_{\mathrm{x}} = |\pm\rangle \tag{50}$$

$$|\pm 1\rangle_{\mathrm{y}} = \frac{|+\rangle \mp \imath\,|-\rangle}{\sqrt{2}} \tag{51}$$

$$|\pm 1\rangle_{\mathrm{z}} = |\tfrac{1}{2}\,(1 \mp 1)\rangle \tag{52}$$

where $|\pm\rangle = (|0\rangle \pm |1\rangle)/\sqrt{2}$ are the x-basis (Hadamard-basis

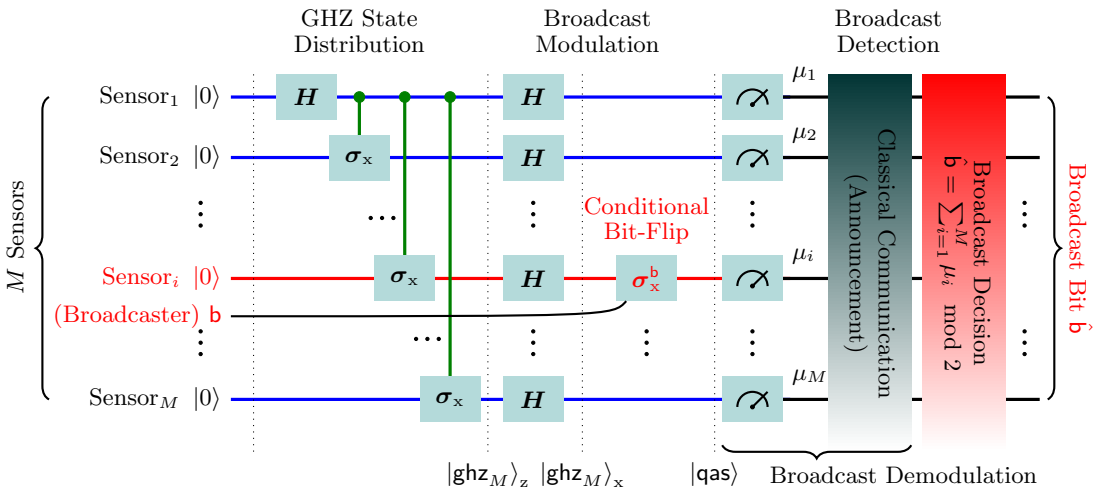

Fig. 9. QAB protocol for QAS broadcast.

or bit-flip) states. Let $|\mathsf{ghz}_N\rangle_{\mathrm{v}}$ be the v-basis GHZ state of N qubits, given by

$$|\mathsf{ghz}_N\rangle_{\mathrm{v}} = \frac{1}{\sqrt{2}}\left(|+1\rangle_{\mathrm{v}}^{\otimes N} + |-1\rangle_{\mathrm{v}}^{\otimes N}\right) \tag{53}$$

for $\mathrm{v} \in \{\mathrm{x}, \mathrm{y}, \mathrm{z}\}$. Now, we consider the probe state for the three-dimensional magnetic field with the unnormalized version as follows [54]:

$$|\boldsymbol{\phi}(\boldsymbol{\theta})\rangle = |\mathsf{ghz}_N\rangle_{\mathrm{x}} + e^{-\imath\theta_1}|\mathsf{ghz}_N\rangle_{\mathrm{y}} + e^{-\imath\theta_2}|\mathsf{ghz}_N\rangle_{\mathrm{z}} \tag{54}$$

Then, the normalized probe state is given by

$$|\boldsymbol{\psi}(\boldsymbol{\theta})\rangle = \frac{|\boldsymbol{\phi}(\boldsymbol{\theta})\rangle}{|\langle\boldsymbol{\phi}(\boldsymbol{\theta})|\boldsymbol{\phi}(\boldsymbol{\theta})\rangle|}. \tag{55}$$

When $N = 4n$ for a positive integer n, by setting the angle $\boldsymbol{\theta} = (\theta_1, \theta_2)$ to $\boldsymbol{\theta} = \mathbf{0}$, the variance of the estimator is bounded as [54]

$$\sum_{k=1}^{K} \mathrm{Var}[\hat{\eta}_k] \geq \frac{3 + 6/\mathrm{sinc}^2(\|\boldsymbol{\eta}\|)}{4N(N+2)} \tag{56}$$

where $\mathrm{sinc}(x) = \sin(x)/x$ and $\|\boldsymbol{\eta}\|$ is not an integer multiple of π. For noisy cases, the purity of the probe state $|\boldsymbol{\psi}(\boldsymbol{\theta})\rangle$ is decreased, rendering it to be mixed (which is described by the density matrix $|\boldsymbol{\psi}(\boldsymbol{\theta})\rangle\langle\boldsymbol{\psi}(\boldsymbol{\theta})|$), and tailored variationally using the PQC designed by the GA. Let

$$\boldsymbol{\rho}(\boldsymbol{\theta}) = \begin{cases} |\boldsymbol{\psi}(\boldsymbol{\theta})\rangle, & \text{for noiseless} \\ |\boldsymbol{\psi}(\boldsymbol{\theta})\rangle\langle\boldsymbol{\psi}(\boldsymbol{\theta})|, & \text{for noisy.} \end{cases} \tag{57}$$

Then, the diagonal and off-diagonal entries of the QFIM are approximated from (15) as follows:

$$\Xi_{kk}(\boldsymbol{\rho}(\boldsymbol{\theta})) \approx 8\left(\frac{1 - \sqrt{\mathcal{F}(\boldsymbol{\rho}(\boldsymbol{\theta}), \boldsymbol{\rho}(\boldsymbol{\theta}; \epsilon\boldsymbol{e}_k))}}{\epsilon^2}\right), \tag{58}$$

$$\Xi_{ij}(\boldsymbol{\rho}(\boldsymbol{\theta})) \approx 4\left(\frac{1 - \sqrt{\mathcal{F}(\boldsymbol{\rho}(\boldsymbol{\theta}), \boldsymbol{\rho}(\boldsymbol{\theta}; \epsilon\boldsymbol{e}_i + \epsilon\boldsymbol{e}_j))}}{\epsilon^2}\right) - \frac{\Xi_{ii}(\boldsymbol{\rho}(\boldsymbol{\theta})) + \Xi_{jj}(\boldsymbol{\rho}(\boldsymbol{\theta}))}{2}, \tag{59}$$

and $\Xi_{ij}(\boldsymbol{\rho}(\boldsymbol{\theta})) = \Xi_{ji}(\boldsymbol{\rho}(\boldsymbol{\theta}))$ due to the symmetric property of the QFIM, where $\boldsymbol{e}_k$ is the kth row of the identity operator in the parameter space. It has been known that when the noise is aligned with the magnetic field, the probe state in the form of (55) cannot surpass the SQL for a constant decay rate [55].

Numerical Examples: Figs. 6–8 show the QCRBs for vector magnetic-field sensing with the VQS, GHZ, and product probe states when $N = 2, 3, 4, 5$, and 6 under the bit-flip, dephasing, and amplitude-damping noises as in Figs. 2–4. For this multiparameter sensing, we set $q = 20$, $r = 3$, and $s = 5$ for the GA to optimize the PQC structure for VQS. We denote (55) simply by the GHZ state and generate the product state as

$$|\boldsymbol{\psi}(\boldsymbol{\theta})\rangle = \left(\frac{|\boldsymbol{\phi}(\boldsymbol{\theta})\rangle}{|\langle\boldsymbol{\phi}(\boldsymbol{\theta})|\boldsymbol{\phi}(\boldsymbol{\theta})\rangle|}\right)^{\otimes N} \tag{60}$$

where

$$|\boldsymbol{\phi}(\boldsymbol{\theta})\rangle = |\mathsf{ghz}_1\rangle_{\mathrm{x}} + e^{-\imath\theta_1}|\mathsf{ghz}_1\rangle_{\mathrm{y}} + e^{-\imath\theta_2}|\mathsf{ghz}_1\rangle_{\mathrm{z}}. \tag{61}$$

We also optimize the parameters $\boldsymbol{\theta}$ of these GHZ and product states for comparison. Similarly, the VQS probe states show improved precision bounds for all three types of noise, and all the probe states are more robust against amplitude-damping noise. The bit-flip and dephasing noises degrade the QCRB in a comparable way and the GHZ state is more robust than the product state in these types of noise. In contrast, the product probe state is more robust than the GHZ state in the amplitude-damping noise.

B. QAS Broadcast

To anonymously share the sensing information obtained by VQS among all the sensors in the QAS network, we employ the QAB protocol that ensures anonymity and untraceability in the broadcast process even when the global quantum state is completely known to other sensors.

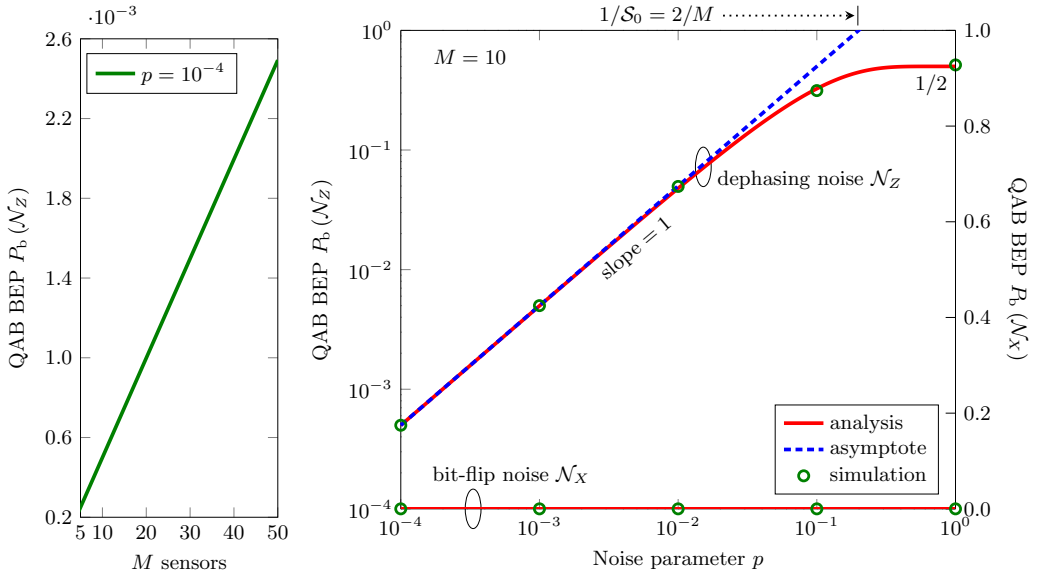

Fig. 10. Broadcast BEP $P_{\mathrm{b}}(\mathcal{N})$ for the QAB protocol as a function of the noise parameter p when $M = 10$ (right) and as a function of the number M of sensing nodes when $p = 10^{-4}$ (left) under bit-flip noise $\mathcal{N}_X$ and dephasing noise $\mathcal{N}_Z$. For simulations, we use the NetSquid designed for quantum network simulations.

1) QAB Protocol: The QAB protocol allows any network sensor to anonymously broadcast its sensing information without revealing its identity. To modulate (encode) the information $\mathsf{b} \in \mathbb{Z}_2 = \{0, 1\}$ on its qubit, the broadcasting sensor flips the x-basis state by applying $\boldsymbol{\sigma}_{\mathrm{x}}^{\mathsf{b}}$. Specifically, the QAB protocol takes a series of steps as follows (see Fig. 9).

Broadcast Preparation: The QAS broadcast protocol starts by preparing an M-qubit GHZ-type state in the x-basis that is shared among all sensor nodes. The M-qubit (z-basis) GHZ state is generated from the state $|0\rangle^{\otimes M}$ as

$$|\mathsf{ghz}_M\rangle_{\mathrm{z}} = \boldsymbol{G}_M \cdots \boldsymbol{G}_2 \boldsymbol{G}_1 |0\rangle^{\otimes M}. \tag{62}$$

After the z-basis GHZ state is shared among all M sensors, each sensor applies the Hadamard operator $\boldsymbol{H}$ to its qubit to prepare the x-basis GHZ state as follows:

$$\begin{aligned} |\mathsf{ghz}_M\rangle_{\mathrm{x}} &= \boldsymbol{H}^{\otimes M} |\mathsf{ghz}_M\rangle_{\mathrm{z}} \\ &= \frac{1}{\sqrt{2}} \left(|+\rangle^{\otimes M} + |-\rangle^{\otimes M} \right) \\ &= \frac{1}{\sqrt{2^{M+1}}} \sum_{\boldsymbol{x} \in \mathbb{Z}_2^M} \left(|\boldsymbol{x}\rangle + (-1)^{\mathrm{sum}_2(\boldsymbol{x})} |\boldsymbol{x}\rangle \right) \\ &= \frac{1}{\sqrt{2^{M-1}}} \sum_{\boldsymbol{x} \in \mathbb{Z}_2^M(0)} |\boldsymbol{x}\rangle \end{aligned} \tag{63}$$

where $\mathbb{Z}_2^M(b)$ represents the set of M-tuple binary sequences (or vectors) with $\mathrm{sum}_2(\boldsymbol{x}) = b \in \mathbb{Z}_2$ and

$$\mathrm{sum}_2(\boldsymbol{x}) = \sum_{j=1}^{M} x_j \mod 2 \tag{64}$$

denotes the modulo 2 addition of all the elements in the binary sequence (or vector) $\boldsymbol{x} = (x_1, x_2, \ldots, x_M) \in \mathbb{Z}_2^M$.

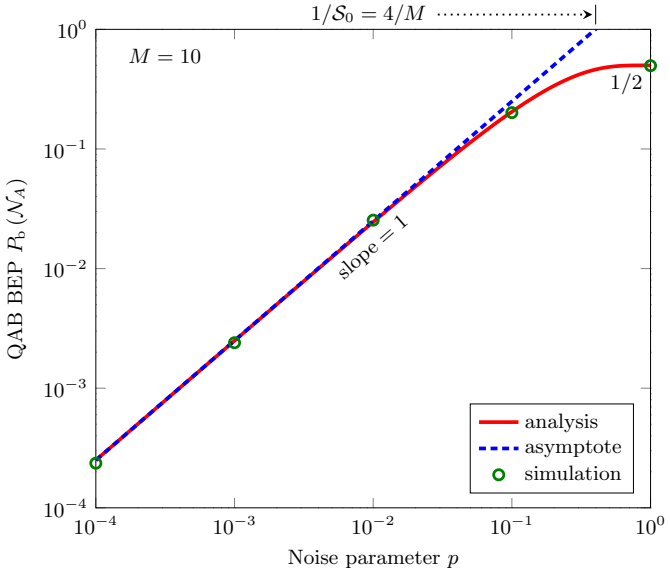

Fig. 11. Broadcast BEP $P_{\mathrm{b}}(\mathcal{N}_A)$ for the QAB protocol as a function of the noise parameter p under amplitude-damping noise $\mathcal{N}_A$ when $M = 10$.

Broadcast Modulation: Let the ith sensor want to broadcast its sensing information $\mathsf{b} \in \mathbb{Z}_2$ to all the network sensors, where $i \in \{1, 2, \ldots, M\}$. Then, the ith sensor modulates the broadcast bit b on its qubit by performing the conditional bit-flip Pauli $\boldsymbol{\sigma}_{\mathrm{x}}^{\mathsf{b}}$. This broadcast modulation transforms the x-basis GHZ state to the QAS broadcast state

$$\begin{aligned} |\mathsf{qas}\rangle &= \boldsymbol{X}_{i,M}^{\mathsf{b}} |\mathsf{ghz}_M\rangle_{\mathrm{x}} \\ &= \frac{1}{\sqrt{2^{M-1}}} \sum_{\boldsymbol{x} \in \mathbb{Z}_2^M(\mathsf{b})} |\boldsymbol{x}\rangle. \end{aligned} \tag{65}$$

Note that the modulated state $|\mathsf{qas}\rangle$ is in the even superposition of all $|\boldsymbol{x}\rangle = |x_1 x_2 \cdots x_M\rangle$ with the modulo 2 sum equal to

the broadcast information b. Since this broadcast-modulated state does not depend on the sensor index i and completely hides the broadcasting sensor's identity, the protocol ensures anonymity and untraceability in the QAS network.

Broadcast Detection: All the M network sensors measure their respective qubits in the computational basis and obtain binary measurement outcomes $\mu_1, \mu_2, \ldots, \mu_M$. This M-tuple binary outcome sequence $\boldsymbol{\mu} = (\mu_1, \mu_2, \ldots, \mu_M) \in \mathbb{Z}_2^M$ appears randomly with an equal probability of $1/2^{M-1}$ due to the x-basis change from the Hadamard operations. However, the modulo sum of all these measurement outcomes is equal to the broadcast sensing information b, i.e., $\mathrm{sum}_2(\boldsymbol{\mu}) = \mathsf{b}$—by the symmetry of the state $|\mathsf{qas}\rangle$ due to the bit-flip modulation. Now, all network sensors announce their measurement outcomes by classical communication. Finally, all $M-1$ recipient sensors recover the sensing information with probability 1 as

$$\hat{\mathsf{b}} = \mathrm{sum}_2(\boldsymbol{\mu}) \tag{66}$$

without revealing the identity of the broadcasting sensor.

2) Noisy Broadcast: We analyze the QAB error probability in noisy QSNs, where each qubit of the M-partite GHZ state $|\mathsf{ghz}_M\rangle_{\mathrm{z}}$ possessed by quantum sensors is subject to the local quantum noise. Using again (42)–(48), we consider the well-known anisotropic quantum noise described by the CPTP map in the Kraus operator-sum representation as follows:

$$\mathcal{N}(\boldsymbol{\rho}) = \boldsymbol{E}_0 \boldsymbol{\rho} \boldsymbol{E}_0^\dagger + \boldsymbol{E}_1 \boldsymbol{\rho} \boldsymbol{E}_1^\dagger \tag{67}$$

where Kraus operators $\boldsymbol{E}_0 = \sqrt{1-p/2}\boldsymbol{I}$ and $\boldsymbol{E}_1 = \sqrt{p/2}\boldsymbol{\sigma}_{\mathrm{x}}$ for bit-flip noise $\mathcal{N} = \mathcal{N}_X$; $\boldsymbol{E}_0 = \sqrt{1-p/2}\boldsymbol{I}$ and $\boldsymbol{E}_1 = \sqrt{p/2}\boldsymbol{\sigma}_{\mathrm{z}}$ for dephasing noise $\mathcal{N} = \mathcal{N}_Z$; $\boldsymbol{E}_0 = |0\rangle\langle 0| + \sqrt{1-p}\,|1\rangle\langle 1|$ and $\boldsymbol{E}_1 = \sqrt{p}\,|0\rangle\langle 1|$ for amplitude-damping noise; and $p \in [0,1]$ denotes a noise parameter such that the qubit is *bit-flipped*, *phase-flipped* with probability $p/2$, or *amplitude-damped* (i.e., decaying from state $|1\rangle$ to $|0\rangle$) with probability p while left untouched (no error) with the complementary probability. Note that the noise parameter p in Kraus operators is related to the decay rate γ_i in the Lindblad master equation as follows:

$$p = \begin{cases} 1 - e^{-2\gamma_i t}, & \text{bit-flip, dephasing} \\ 1 - e^{-\gamma_i t}, & \text{amplitude-damping.} \end{cases} \tag{68}$$

The broadcast BEP for the QAB protocol under quantum noise $\mathcal{N}$ is given by

$$P_{\mathrm{b}}(\mathcal{N}) = \sum_{i \in \mathbb{Z}_2} \Pr\big[\hat{\mathsf{b}} \neq \mathsf{b} \big| \mathsf{b} = i, \boldsymbol{\rho}(\mathcal{N})\big] \Pr[\mathsf{b} = i] \tag{69}$$

$$= \begin{cases} 0, & \text{bit-flip} \\ \frac{1}{2} - \frac{1}{2}(1-p)^M, & \text{dephasing} \\ \frac{1}{2} - \frac{1}{2}(1-p)^{M/2}, & \text{amplitude-damping} \end{cases} \tag{70}$$

where all derivations are relegated to the Appendix and

$$\boldsymbol{\rho}(\mathcal{N}) = \mathcal{N}^{\otimes M}\left(|\mathsf{ghz}_M\rangle_{\mathrm{z}}\langle \mathsf{ghz}_M|\right) = \frac{1}{2}\sum_{i,j \in \mathbb{Z}_2} \mathcal{N}\left(|i\rangle\langle j|\right)^{\otimes M} \tag{71}$$

is the noisy z-state GHZ state prepared for the QAS broadcast. Note that the *error-free* resilience of the QAB protocol under bit-flip noise is due to the fact that this noise leaves the qubit's phase unchanged, only bit-flipping its state. Projecting $|i\rangle\langle j|$ in x-basis is equal to projecting the bit-flipped version of $|i\rangle\langle j|$ in x-basis, i.e., $\langle \pm|\boldsymbol{\sigma}_{\mathrm{x}}|i\rangle\langle j|\boldsymbol{\sigma}_{\mathrm{x}}|\pm\rangle = \langle \pm|i\rangle\langle j|\pm\rangle$, since $|\pm\rangle$ are the eigenvectors of $\boldsymbol{\sigma}_{\mathrm{x}}$ corresponding to ± 1 eigenvalues.

In the low-noise regime, the QAB error probability $P_{\mathrm{b}}(\mathcal{N})$ behaves as

$$P_{\mathrm{b}}(\mathcal{N}) = p\mathcal{S}_0 + o(p) \qquad (p \to 0) \tag{72}$$

where

$$\mathcal{S}_0 = \lim_{p \to 0} \frac{P_{\mathrm{b}}(\mathcal{N})}{p} = \begin{cases} M/2, & \text{dephasing} \\ M/4, & \text{amplitude-damping.} \end{cases} \tag{73}$$

This asymptotic BEP behavior reveals that the low-noise slope of $P_{\mathrm{b}}(\mathcal{N})$ as a function of p in a log-log plot is equal to one, while the quantity $1/\mathcal{S}_0$ represents the low-noise offset in the BEP asymptote as $p \to 0$—that is, $P_{\mathrm{b}}(\mathcal{N})$ scales linearly with the dephasing or damping probability p and the network size M in the low-noise regime (see Figs. 10 and 11).

VI. Conclusion

Emerging applications in wireless networks demand ultra-precise and ultra-secure ISAC solutions. Quantum advantages improve classical precision scaling and provide unconditional security. However, the near-term quantum devices face practical challenges, such as inherent quantum noise that hinders their achievable potential. In this paper, we have developed genetic VQS to optimize sensing configurations variationally and evolutionarily in noisy environments. This GA approach finds the fittest PQC structure that effectively combats quantum noise, such as well-known bit-flip, dephasing, and amplitude-damping noises. The PQC parameters are adjusted to create a high-quality variational sensing probe state that maximizes the QFI in resilience to quantum noise for both single-parameter and multiparameter sensing. Moreover, we integrate the QAB protocol into VQS networks to anonymously share sensing information among all network parties, ensuring anonymity and untraceability of sensing data. This QAS broadcast has error-free resilience against the bit-flip noise, while its asymptotic BEP linearly scales with the network size and the dephasing or damping probability under dephasing and amplitude-damping noises in the low-noise regime. This work serves to put forth the NISQ ISAC framework specifically in a variational and anonymous manner.

Appendix
Broadcast Error Probability

Due to the symmetry, the broadcast BEP $P_{\mathrm{b}}(\mathcal{N})$ in (69) for equiprobable *a priori* broadcast information, i.e., $\Pr[\mathsf{b}=0] = \Pr[\mathsf{b}=1] = 1/2$, can be written as

$$P_{\mathrm{b}}(\mathcal{N}) = \Pr\big[\hat{\mathsf{b}} = 1 \big| \mathsf{b} = 0, \boldsymbol{\rho}(\mathcal{N})\big]. \tag{74}$$

Hence, we only consider the case $\mathsf{b} = 0$ to derive the BEP, for which the QAB modulation and demodulation are equivalent

to measuring M qubits of the noisy state $\boldsymbol{\rho}(\mathcal{N})$ *locally* in x-basis and calculating the modulo sum of outcomes $\boldsymbol{\mu} \in \mathbb{Z}_2^M$, i.e., $\mathrm{sum}_2(\boldsymbol{\mu})$. If the qubit collapses to $|+\rangle$ or $|-\rangle$, the x-basis measurement outcome is 0 or 1.

A. Bit-Flip Noise

The x-basis projection and bit-flip noise map $\mathcal{N}_X$ of $|i\rangle\langle j|$ for $i, j \in \mathbb{Z}_2$ are given by

$$\langle \pm|i\rangle\langle j|\pm\rangle = (-1)^{i\mp j}\, 1/2 \tag{75}$$

$$\mathcal{N}_X(|i\rangle\langle j|) = (1-p/2)\,|i\rangle\langle j| + p/2\,|1-i\rangle\langle 1-j|\,. \tag{76}$$

Using (71), (75), and (76), we have the measurement outcome probability of $\boldsymbol{\mu} \in \mathbb{Z}_2^M(0)$ for the bit-flip noisy GHZ state as follows:

$$\Pr\big[\boldsymbol{\mu} \in \mathbb{Z}_2^M(0)\,\big|\,\boldsymbol{\rho}(\mathcal{N}_X)\big] = \frac{1}{2^{M-1}}. \tag{77}$$

Hence, with 2^{M-1} possible sequences, we obtain the broadcast detecting probability under bit-flip noise $\mathcal{N}_X$ as

$$\Pr\big[\mathrm{sum}_2(\boldsymbol{\mu}) = 0\big|\mathsf{b} = 0, \boldsymbol{\rho}(\mathcal{N}_X)\big] = 1, \tag{78}$$

leading to the zero BEP in the first case of (70).

B. Dephasing Noise

Using (71), (75), and the dephasing noise maps $\mathcal{N}_Z$ of diagonal $|i\rangle\langle i|$ and non-diagonal $|i\rangle\langle 1-i|$ states

$$\mathcal{N}_Z(|i\rangle\langle i|) = |i\rangle\langle i| \tag{79}$$

$$\mathcal{N}_Z(|i\rangle\langle 1-i|) = (1-p)\,|i\rangle\langle 1-i| \tag{80}$$

for $i \in \mathbb{Z}_2$, we have

$$\Pr\big[\boldsymbol{\mu} \in \mathbb{Z}_2^M(0)\,\big|\,\boldsymbol{\rho}(\mathcal{N}_Z)\big] = \frac{1+(1-p)^M}{2^M}. \tag{81}$$

Again, with 2^{M-1} possible sequences, we obtain the broadcast detecting probability under dephasing noise $\mathcal{N}_Z$ as follows:

$$\Pr\big[\mathrm{sum}_2(\boldsymbol{\mu}) = 0\big|\mathsf{b} = 0, \boldsymbol{\rho}(\mathcal{N}_Z)\big] = \frac{1+(1-p)^M}{2}, \tag{82}$$

leading to the broadcast BEP in the second case of (70).

C. Amplitude-Damping Noise

Similarly, since the amplitude-damping noise maps $\mathcal{N}_A$ of diagonal $|i\rangle\langle i|$ and non-diagonal $|i\rangle\langle 1-i|$ states for $i \in \mathbb{Z}_2$ are given by

$$\mathcal{N}_A(|0\rangle\langle 0|) = |0\rangle\langle 0| \tag{83}$$

$$\mathcal{N}_A(|1\rangle\langle 1|) = p\,|0\rangle\langle 0| + (1-p)\,|1\rangle\langle 1| \tag{84}$$

$$\mathcal{N}_A(|i\rangle\langle 1-i|) = \sqrt{1-p}\,|i\rangle\langle 1-i|\,, \tag{85}$$

we obtain the broadcast detecting probability under amplitude-damping noise $\mathcal{N}_A$ as

$$\Pr\big[\mathrm{sum}_2(\boldsymbol{\mu}) = 0\big|\mathsf{b} = 0, \boldsymbol{\rho}(\mathcal{N}_A)\big] = \frac{1+(1-p)^{M/2}}{2}, \tag{86}$$

leading to the QAB BEP in the third case of (70).

REFERENCES

[1] Z. Wang, Z. Liu, Y. Shen, A. Conti, and M. Z. Win, "Location awareness in beyond 5G networks via reconfigurable intelligent surfaces," *IEEE J. Sel. Areas Commun.*, vol. 40, no. 7, pp. 2011–2025, Jul. 2022.

[2] A. Conti, F. Morselli, Z. Liu, S. Bartoletti, S. Mazuelas, W. C. Lindsey, and M. Z. Win, "Location awareness in beyond 5G networks," *IEEE Commun. Mag.*, vol. 59, no. 11, pp. 22–27, Nov. 2021.

[3] A. Conti, S. Mazuelas, S. Bartoletti, W. C. Lindsey, and M. Z. Win, "Soft information for localization-of-things," *Proc. IEEE*, vol. 107, no. 11, pp. 2240–2264, Nov. 2019.

[4] M. Z. Win, W. Dai, Y. Shen, G. Chrisikos, and H. Vincent Poor, "Network operation strategies for efficient localization and navigation," *Proc. IEEE*, vol. 106, no. 7, pp. 1224–1254, Jul. 2018.

[5] F. Meyer, T. Kropfreiter, J. L. Williams, R. Lau, F. Hlawatsch, P. Braca, and M. Z. Win, "Message passing algorithms for scalable multitarget tracking," *Proc. IEEE*, vol. 106, no. 2, pp. 221–259, Feb. 2018.

[6] M. Z. Win, F. Meyer, Z. Liu, W. Dai, S. Bartoletti, and A. Conti, "Efficient multisensor localization for the Internet of Things: Exploring a new class of scalable localization algorithms," *IEEE Signal Process. Mag.*, vol. 35, no. 5, pp. 153–167, Sep. 2018.

[7] M. Z. Win, Y. Shen, and W. Dai, "A theoretical foundation of network localization and navigation," *Proc. IEEE*, vol. 106, no. 7, pp. 1136–1165, Jul. 2018.

[8] T. V. Nguyen, Y. Jeong, H. Shin, and M. Z. Win, "Machine learning for wideband localization," *IEEE J. Sel. Areas Commun.*, vol. 33, no. 7, pp. 1357–1380, Jul. 2015.

[9] R. Du, C. Chen, B. Yang, N. Lu, X. Guan, and X. Shen, "Effective urban traffic monitoring by vehicular sensor networks," *IEEE Trans. Veh. Technol.*, vol. 64, no. 1, pp. 273–286, Jan. 2015.

[10] F. Tang, X. Chen, M. Zhao, and N. Kato, "The roadmap of communication and networking in 6G for the Metaverse," *IEEE Wireless Commun.*, vol. 30, no. 4, pp. 72–81, Jun. 2023.

[11] Z. Zhu, C. Guo, R. Bao, M. Chen, W. Saad, and Y. Yang, "Positioning using visible light communications: A perspective arcs approach," *IEEE Trans. Wireless Commun.*, vol. 22, no. 10, pp. 6962–6977, Mar. 2023.

[12] M. Cheng, Q. Guan, F. Ji, J. Cheng, and Y. Chen, "Dynamic-detection-based trajectory planning for autonomous underwater vehicle to collect data from underwater sensors," *IEEE Internet Things J.*, vol. 9, no. 15, pp. 13 168–13 178, Jan. 2022.

[13] L. Bai, Y. Yang, Z. Zhang, C. Feng, C. Guo, and J. Cheng, "A high-coverage camera assisted received signal strength ratio algorithm for indoor visible light positioning," *IEEE Trans. Wireless Commun.*, vol. 20, no. 9, pp. 5730–5743, Apr. 2021.

[14] A. Liu, Z. Huang, M. Li, Y. Wan, W. Li, T. X. Han, C. Liu, R. Du, D. K. P. Tan, J. Lu, Y. Shen, F. Colone, and K. Chetty, "A survey on fundamental limits of integrated sensing and communication," *IEEE Commun. Surveys Tuts.*, vol. 24, no. 2, pp. 994–1034, Feb. 2022.

[15] Q. Nhat Le, V.-D. Nguyen, O. A. Dobre, and H. Shin, "RIS-assisted full-duplex integrated sensing and communication," *IEEE Wireless Commun. Lett.*, vol. 12, no. 10, pp. 1677–1681, Oct. 2023.

[16] U. Demirhan and A. Alkhateeb, "Integrated sensing and communication for 6G: Ten key machine learning roles," *IEEE Commun. Mag.*, vol. 61, no. 5, pp. 113–119, May 2023.

[17] Z. Eldredge, M. Foss-Feig, J. A. Gross, S. L. Rolston, and A. V. Gorshkov, "Optimal and secure measurement protocols for quantum sensor networks," *Phys. Rev. A*, vol. 97, no. 4, p. 042337, Apr. 2018.

[18] N. Aslam, H. Zhou, E. K. Urbach, M. J. Turner, R. L. Walsworth, M. D. Lukin, and H. Park, "Quantum sensors for biomedical applications," *Nat. Rev. Phys.*, vol. 5, no. 3, pp. 157–169, Feb. 2023.

[19] H. Wang, H. Ning, Y. Lin, W. Wang, S. Dhelim, F. Farha, J. Ding, and M. Daneshmand, "A survey on the Metaverse: The state-of-the-art, technologies, applications, and challenges," *IEEE Internet Things J.*, vol. 10, no. 16, pp. 14 671–14 688, 2023.

[20] H. Yu, D. Martynov, R. X. Adhikari, and Y. Chen, "Exposing gravitational waves below the quantum sensing limit," *Phys. Rev. D*, vol. 106, no. 6, p. 063017, Sep. 2022.

[21] F. Zaman, U. Khalid, T. Q. Duong, H. Shin, and M. Z. Win, "Quantum full-duplex communication," *IEEE J. Sel. Areas Commun.*, vol. 41, no. 9, pp. 2966–2980, Sep. 2023.

[22] U. Khalid, M. S. Ulum, A. Farooq, T. Q. Duong, O. A. Dobre, and H. Shin, "Quantum semantic communications for Metaverse: Principles and challenges," *IEEE Wireless Commun.*, vol. 30, no. 4, pp. 26–36, Aug. 2023.

[23] U. Khalid, J. ur Rehman, and H. Shin, "Metrologically resourceful multipartite entanglement under quantum many-body effects," *Quantum Sci. Technol.*, vol. 6, no. 2, p. 025007, Jan. 2021.

[24] G. Wang, A. R. Barr, H. Tang *et al.*, "Characterizing temperature and strain variations with qubit ensembles for their robust coherence protection," *Phys. Rev. Lett.*, vol. 131, no. 4, p. 043602, Jul. 2023.
[25] K. Yamamoto, S. Endo, H. Hakoshima *et al.*, "Error-mitigated quantum metrology via virtual purification," *Phys. Rev. Lett.*, vol. 129, no. 25, p. 250503, Dec. 2022.
[26] Z. Liu, K.-K. R. Choo, and J. Grossschadl, "Securing edge devices in the post-quantum Internet of Things using lattice-based cryptography," *IEEE Commun. Mag.*, vol. 56, no. 2, pp. 158–162, Feb. 2018.
[27] U. Khalid, J. u. Rehman, S. N. Paing, H. Jung, T. Q. Duong, and H. Shin, "Quantum network engineering in the NISQ age: Principles, missions, and challenges," *IEEE Netw.*, early access, Oct 31, 2023, doi:10.1109/MNET.2023.3328892.
[28] F. Zaman, A. Farooq, M. A. Ullah, H. Jung, H. Shin, and M. Z. Win, "Quantum machine intelligence for 6G URLLC," *IEEE Wireless Commun.*, vol. 30, no. 2, pp. 22–30, Apr. 2023.
[29] S. N. Paing, J. W. Setiawan, M. A. Ullah, F. Zaman, T. Q. Duong, O. A. Dobre, and H. Shin, "Counterfactual quantum Byzantine consensus for human-centric Metaverse," *IEEE J. Sel. Areas Commun.*, to be published.
[30] C. D. Marciniak, T. Feldker, I. Pogorelov, R. Kaubruegger, D. V. Vasilyev, R. van Bijnen, P. Schindler, P. Zoller, R. Blatt, and T. Monz, "Optimal metrology with programmable quantum sensors," *Nature*, vol. 603, no. 7902, pp. 604–609, Mar. 2022.
[31] R. Kaubruegger, D. V. Vasilyev, M. Schulte, K. Hammerer, and P. Zoller, "Quantum variational optimization of Ramsey interferometry and atomic clocks," *Phys. Rev. X*, vol. 11, no. 4, p. 041045, Dec. 2021.
[32] H. Huo, M. Zhuang, J. Huang, and C. Lee, "Machine optimized quantum metrology of concurrent entanglement generation and sensing," *Quantum Sci. Technol.*, vol. 7, no. 2, p. 025010, Mar. 2022.
[33] M. Cerezo, A. Arrasmith, R. Babbush, S. C. Benjamin, S. Endo, K. Fujii, J. R. McClean, K. Mitarai, X. Yuan, L. Cincio *et al.*, "Variational quantum algorithms," *Nat. Rev. Phys.*, vol. 3, no. 9, pp. 625–644, Aug. 2021.
[34] J. Yang, S. Pang, Z. Chen, A. N. Jordan, and A. del Campo, "Variational principle for optimal quantum controls in quantum metrology," *Phys. Rev. Lett.*, vol. 128, no. 16, p. 160505, Apr. 2022.
[35] B. Koczor, S. Endo, T. Jones, Y. Matsuzaki, and S. C. Benjamin, "Variational-state quantum metrology," *New J. Phys.*, vol. 22, no. 8, p. 083038, Aug. 2020.
[36] Y. Zhou, Y. Fang, and Y. Zhang, "Securing wireless sensor networks: A survey," *IEEE Commun. Surveys Tuts.*, vol. 10, no. 3, pp. 6–28, Sep. 2008.
[37] X. Du and H.-h. Chen, "Security in wireless sensor networks," *IEEE Wireless Commun.*, vol. 15, no. 4, pp. 60–66, Aug. 2008.
[38] A. Khan, U. Khalid, J. ur Rehman, and H. Shin, "Quantum anonymous private information retrieval for distributed networks," *IEEE Trans. Commun.*, vol. 70, no. 6, pp. 4026–4037, Jun. 2022.
[39] A. Khan, U. Khalid, J. ur Rehman, K. Lee, and H. Shin, "Quantum anonymous collision detection for quantum networks," *EPJ Quantum Technol.*, vol. 8, no. 1, p. 27, Dec. 2021.
[40] A. Khan, J. ur Rehman, and H. Shin, "Quantum anonymous notification for network-based applications," *Quantum Inf. Process.*, vol. 20, no. 12, p. 397, Nov. 2021.
[41] F. Zaman, S. N. Paing, A. Farooq, H. Shin, and M. Z. Win, "Concealed quantum telecomputation for anonymous 6G URLLC networks," *IEEE J. Sel. Areas Commun.*, vol. 41, no. 7, pp. 2278–2296, Jul. 2023.
[42] M. Cerezo, A. Sone, J. L. Beckey, and P. J. Coles, "Sub-quantum Fisher information," *Quantum Sci. Technol.*, vol. 6, no. 3, p. 035008, Jun. 2021.
[43] J. Liu, H. Yuan, X.-M. Lu, and X. Wang, "Quantum Fisher information matrix and multiparameter estimation," *J. Phys. A-Math. Theor.*, vol. 53, no. 2, p. 023001, Dec. 2019.
[44] J. J. Meyer, "Fisher information in noisy intermediate-scale quantum applications," *Quantum*, vol. 5, p. 539, Sep. 2021.
[45] L. Bittel and M. Kliesch, "Training variational quantum algorithms is NP-hard," *Phys. Rev. Lett.*, vol. 127, no. 12, p. 120502, Sep. 2021.
[46] M. Schuld, V. Bergholm, C. Gogolin, J. Izaac, and N. Killoran, "Evaluating analytic gradients on quantum hardware," *Phys. Rev. A*, vol. 99, no. 3, p. 032331, Mar. 2019.
[47] R. Sweke, F. Wilde, J. Meyer, M. Schuld, P. K. Faehrmann, B. Meynard-Piganeau, and J. Eisert, "Stochastic gradient descent for hybrid quantum-classical optimization," *Quantum*, vol. 4, p. 314, Aug. 2020.
[48] D. P. Kingma and J. Ba, "Adam: A method for stochastic optimization," *arXiv:1412.6980*, Jan. 2017.
[49] X. Ge, R.-B. Wu, and H. Rabitz, "The optimization landscape of hybrid quantum–classical algorithms: From quantum control to NISQ applications," *Annu. Rev. Control*, vol. 54, pp. 314–323, Nov. 2022.
[50] J. Romero, R. Babbush, J. R. McClean, C. Hempel, P. J. Love, and A. Aspuru-Guzik, "Strategies for quantum computing molecular energies using the unitary coupled cluster ansatz," *Quantum Science and Technology*, vol. 4, no. 1, p. 014008, Oct. 2018.
[51] S. Y.-C. Chen, C.-M. Huang, C.-W. Hsing, H.-S. Goan, and Y.-J. Kao, "Variational quantum reinforcement learning via evolutionary optimization," *Mach. Learn.-Sci. Technol.*, vol. 3, no. 1, p. 015025, Feb. 2022.
[52] T. Rindell, B. Yenilen, N. Halonen, A. Pönni, I. Tittonen, and M. Raasakka, "Exploring the optimality of approximate state preparation quantum circuits with a genetic algorithm," *Phys. Lett. A*, vol. 475, p. 128860, Jul. 2023.
[53] A. Kenfack and K. Życzkowski, "Negativity of the Wigner function as an indicator of non-classicality," *J. Opt. B-Quantum Semicl. Opt.*, vol. 6, no. 10, p. 396, Aug. 2004.
[54] T. Baumgratz and A. Datta, "Quantum enhanced estimation of a multidimensional field," *Phys. Rev. Lett.*, vol. 116, no. 3, p. 030801, Jan. 2016.
[55] L. B. Ho, H. Hakoshima, Y. Matsuzaki, M. Matsuzaki, and Y. Kondo, "Multiparameter quantum estimation under dephasing noise," *Phys. Rev. A*, vol. 102, no. 2, p. 022602, Aug 2020.